Inclusive electron scattering in the resonance region off a hydrogen target with CLAS12

```
V. Klimenko , <sup>7,1</sup> D. S. Carman , <sup>4</sup> R. W. Gothe , <sup>3</sup> K. Joo, <sup>7</sup> N. Markov, <sup>7,4</sup> V. I. Mokeev , <sup>4</sup> G. Niculescu , <sup>23</sup>
    P. Achenbach, <sup>41</sup> J. S. Alvarado, <sup>33</sup> W. Armstrong, <sup>1</sup> H. Atac, <sup>39</sup> H. Avakian, <sup>41</sup> L. Baashen, <sup>24</sup> N. A. Baltzell, <sup>41</sup> L. Barion, <sup>16</sup> M. Bashkanov, <sup>44</sup> M. Battaglieri, <sup>18</sup> F. Benmokhtar, <sup>9</sup> A. Bianconi, <sup>2,19</sup> A. S. Biselli, <sup>10</sup> S. Boiarinov, <sup>41</sup> F. Bossù, <sup>36</sup> K.-Th. Brinkmann, <sup>22</sup> W. J. Briscoe, <sup>14</sup> W. K. Brooks, <sup>40</sup> V. D. Burkert, <sup>41</sup> S. Bueltmann, <sup>32</sup> R. Capobianco, <sup>7</sup> J. Carvajal, <sup>12</sup> A. Celentano, <sup>18</sup> P. Chatagnon, <sup>36,33</sup> G. Ciullo, <sup>16,11</sup> A. D'Angelo, <sup>20,35</sup> N. Dashyan, <sup>43</sup> M. Defurne, <sup>36</sup> R. De Vita, <sup>18,41</sup> A. Deur, <sup>41</sup> S. Diehl, <sup>22,7</sup> C. Dilks, <sup>41</sup> C. Djalali, <sup>31</sup> R. Dupré, <sup>33</sup> H. Egiyan, <sup>41</sup> A. El Alaoui, <sup>40</sup> L. El Fassi, <sup>27</sup> L. Elouadrhiri, <sup>41</sup> S. Fegan, <sup>44</sup> L. B. Ferrando, <sup>42</sup> A. Ellingi, <sup>21</sup> G. Genelin, <sup>41</sup> C. B. Cillo, <sup>13</sup> R. Dupré, <sup>33</sup> P. L. Elouadrhiri, <sup>41</sup> S. Fegan, <sup>44</sup> L. B. Ferrando, <sup>42</sup> A. Ellingi, <sup>21</sup> G. Genelin, <sup>41</sup> C. B. Cillo, <sup>13</sup> R. Dupré, <sup>33</sup> P. L. Charles, <sup>43</sup> R. L. Elouadrhiri, <sup>41</sup> S. Fegan, <sup>44</sup> R. L. Ellingi, <sup>21</sup> G. Genelin, <sup>41</sup> C. R. Cillo, <sup>13</sup> R. Dupré, <sup>33</sup> P. L. Charles, <sup>43</sup> R. L. Ellingi, <sup>43</sup> R. Dupré, <sup>33</sup> R. Dupré, <sup>33</sup> R. Dupré, <sup>34</sup> R. L. Charles, <sup>44</sup> R. L. Ellingi, <sup>45</sup> R. Charles, <sup>46</sup> R. R. L. Charles, <sup>46</sup> R. R. L. Charles, <sup>47</sup> R. L. Charles, <sup>48</sup> R. L. Charles, <sup>48</sup> R. L. Charles, <sup>48</sup> R. L. Charles, <sup>49</sup> R. L. Charles, <sup>49</sup> R. L. Charles, <sup>49</sup> R. L. Charles, <sup>49</sup> R. L. Charles, <sup>40</sup> R. L. Charles, <sup>49</sup> R. L. Charles, <sup>40</sup> R. L. Charles, <sup>49</sup> R. L. Charles, <sup>49</sup>
   S. Dieni, <sup>5,5</sup> C. Djalali, <sup>5,6</sup> R. Dupré, <sup>5,5</sup> H. Egiyan, <sup>5,6</sup> A. El Alaoui, <sup>5,6</sup> L. El Fassi, <sup>2,7</sup> L. Elouadrhiri, <sup>5,1</sup> S. Fegan, <sup>5,6</sup> I. P. Fernando, <sup>4,2</sup> A. Filippi, <sup>2,1</sup> G. Gavalian, <sup>4,1</sup> G. P. Gilfoyle, <sup>3,4</sup> D. I. Glazier, <sup>1,5</sup> K. Hafidi, <sup>1</sup> H. Hakobyan, <sup>4,0</sup> M. Hattawy, <sup>3,2</sup> F. Hauenstein, <sup>4,1</sup> T. B. Hayward, <sup>2,6</sup> D. Heddle, <sup>6,4,1</sup> A. N. Hiller Blin, <sup>4,1</sup> A. Hobart, <sup>3,3</sup> M. Holtrop, <sup>2,8</sup> Y. Ilieva, <sup>3,8</sup> D. G. Ireland, <sup>1,5</sup> E. L. Isupov, <sup>3,7</sup> H. Jiang, <sup>1,5</sup> H. S. Jo, <sup>2,5</sup> S. Joosten, <sup>1,3,9</sup> T. Kageya, <sup>4,1</sup> D. Keller, <sup>4,2</sup> A. Kim, <sup>7</sup> W. Kim, <sup>2,5</sup> H. T. Klest, <sup>1</sup> A. Kripko, <sup>2,2</sup> V. Kubarovsky, <sup>4,1</sup> S. E. Kuhn, <sup>3,2</sup> L. Lanza, <sup>2,0</sup> S. Lee, <sup>1</sup> P. Lenisa, <sup>1,6,11</sup> K. Livingston, <sup>1,5</sup> I. J. D. MacGregor, <sup>1,5</sup> D. Marchand, <sup>3,3</sup> D. Martiryan, <sup>4,3</sup> V. Mascagna, <sup>2,19</sup> D. Matamoris, <sup>3,3</sup> B. McKinnon, <sup>1,5</sup> T. Mineeva, <sup>4,0</sup> M. Mirazita, <sup>1,7</sup> C. Munoz Camacho, <sup>3,3</sup> P. Nadel-Turonski, <sup>3,8,41</sup> T. Nagorna, <sup>1,8</sup> K. Neupane, <sup>3,8</sup> S. Niccolai, <sup>3,3</sup> M. Osipenko, <sup>1,8</sup> M. Paolone, <sup>2,9,39</sup> L. L. Pappalardo, <sup>1,6,11</sup> R. Paramarana, <sup>4,1,28</sup> E. Pappalardo, <sup>1,6,11</sup> N. Pillana, <sup>1,6</sup> D. Palabara, Pagalaka, P
                      R. Paremuzyan, 41,28 E. Pasyuk, 41 S. J. Paul, 3 W. Phelps, 6,41 N. Pilleux, 1 S. Polcher Rafael, 36 J. W. Price, 4 Y. Prok, 32
B. A. Raue, <sup>12</sup> J. Richards, <sup>7</sup> M. Ripani, <sup>18</sup> J. Ritman, <sup>13</sup> P. Rossi, <sup>41,17</sup> A. A. Rusova, <sup>37</sup> C. Salgado, <sup>6,30</sup> S. Schadmand, <sup>13</sup> A. Schmidt, <sup>14,26</sup> Y. G. Sharabian, <sup>41</sup> E. V. Shirokov, <sup>37</sup> S. Shrestha, <sup>39</sup> N. Sparveris, <sup>39</sup> M. Spreafico, <sup>18</sup> S. Stepanyan, <sup>41</sup> I. I. Strakovsky, <sup>14</sup> S. Strauch, <sup>38</sup> J. A Tan, <sup>25</sup> M. Tenorio, <sup>32</sup> N. Trotta, <sup>7</sup> R. Tyson, <sup>41</sup> M. Ungaro, <sup>41</sup> S. Vallarino, <sup>16</sup> L. Venturelli, <sup>2,19</sup> T. Vittorini, <sup>18</sup> H. Voskanyan, <sup>43</sup> E. Voutier, <sup>33</sup> D. P. Watts, <sup>44</sup> U. Weerasinghe, <sup>27</sup> X. Wei, <sup>41</sup> M. H. Wood, <sup>5</sup> L. Xu, <sup>33</sup> N. Zachariou, <sup>44</sup>
                                                                                                                                                                                     Z. W. Zhao,<sup>8</sup> and M. Zurek<sup>1</sup>
                                                                                                                                                                                                (CLAS Collaboration)
                                                                                                                                    <sup>1</sup>Argonne National Laboratory, Argonne, Illinois 60439, USA
                                                                                                                                               <sup>2</sup>Università degli Studi di Brescia, 25123 Brescia, Italy
                                                                              <sup>3</sup>University of California Riverside, 900 University Avenue, Riverside, California 92521, USA
                                                                                                       <sup>4</sup>California State University, Dominguez Hills, Carson, California 90747, USA
                                                                                                                                                      <sup>5</sup>Canisius College, Buffalo, New York 14208, USA
                                                                                                                    <sup>6</sup>Christopher Newport University, Newport News, Virginia 23606, USA
                                                                                                                                       <sup>7</sup>University of Connecticut, Storrs, Connecticut 06269, USA
                                                                                                                                             <sup>8</sup>Duke University, Durham, North Carolina 27708, USA
                                                                                                   <sup>9</sup>Duquesne University, 600 Forbes Avenue, Pittsburgh, Pennsylvania 15282, USA
                                                                                                                                           <sup>10</sup>Fairfield University, Fairfield, Connecticut 06824, USA
                                                                                                                                                               <sup>11</sup>Università di Ferrara, 44121 Ferrara, Italy
                                                                                                                                <sup>12</sup>Florida International University, Miami, Florida 33199, USA
                                                                                    <sup>13</sup>GSI Helmholtzzentrum fur Schwerionenforschung GmbH, D-64291 Darmstadt, Germany
                                                                                                                         <sup>14</sup>The George Washington University, Washington, D.C. 20052, USA
                                                                                                                                  <sup>15</sup>University of Glasgow, Glasgow G12 8QQ, United Kingdom
                                                                                                                                                        <sup>16</sup>INFN, Sezione di Ferrara, 44100 Ferrara, Italy
                                                                                                                                <sup>17</sup>INFN, Laboratori Nazionali di Frascati, 00044 Frascati, Italy
                                                                                                                                                        <sup>18</sup>INFN, Sezione di Genova, 16146 Genova, Italy
                                                                                                                                                               <sup>19</sup>INFN, Sezione di Pavia, 27100 Pavia, Italy
                                                                                                                                          <sup>20</sup>INFN, Sezione di Roma Tor Vergata, 00133 Rome, Italy
                                                                                                                                                            <sup>21</sup>INFN, Sezione di Torino, 10125 Torino, Italy
                                                                                                        <sup>22</sup>II Physikalisches Institut der Universitaet Giessen, 35392 Giessen, Germany
                                                                                                                                       <sup>23</sup> James Madison University, Harrisonburg, Virginia 22807
                                                                                                                             <sup>24</sup>King Saud University, Riyadh, 11362 Kingdom of Saudi Arabia
                                                                                                                       <sup>25</sup>Kyungpook National University, Daegu 702-701, Republic of Korea
                                                                                                    <sup>26</sup>Massachusetts Institute of Technology, Cambridge, Massachusetts 02139, USA
                                                                                                                 <sup>27</sup>Mississippi State University, Mississippi State, Mississippi 39762, USA
                                                                                                                    <sup>28</sup>University of New Hampshire, Durham, New Hampshire 03824, USA
                                                                                                                      <sup>29</sup>New Mexico State University, Las Cruces, New Mexico 88003, USA
                                                                                                                                           <sup>30</sup>Norfolk State University, Norfolk, Virginia 23504, USA
                                                                                                                                                               <sup>31</sup>Ohio University, Athens, Ohio 45701, USA
                                                                                                                                         <sup>32</sup>Old Dominion University, Norfolk, Virginia 23529, USA
```

Published by the American Physical Society under the terms of the Creative Commons Attribution 4.0 International license. Further distribution of this work must maintain attribution to the author(s) and the published article's title, journal citation, and DOI. Funded by SCOAP³.

33 Université Paris-Saclay, CNRS/IN2P3, IJCLab, 91405 Orsay, France
 34 University of Richmond, Richmond, Virginia 23173, USA
 35 Università di Roma Tor Vergata, 00133 Rome, Italy
 36 IRFU, CEA, Université Paris-Saclay, F-91191 Gif-sur-Yvette, France
 37 Skobeltsyn Nuclear Physics Institute and Physics Department at Lomonosov Moscow State University, 119899 Moscow, Russia
 38 University of South Carolina, Columbia, South Carolina 29208, USA
 39 Temple University, Philadelphia, Pennsylvania 19122, USA
 40 Universidad Técnica Federico Santa María, Casilla 110-V Valparaíso, Chile
 41 Thomas Jefferson National Accelerator Facility, Newport News, Virginia 23606, USA
 42 University of Virginia, Charlottesville, Virginia 22901, USA
 43 Yerevan Physics Institute, 375036 Yerevan, Armenia
 44 University of York, York YO10 5DD, United Kingdom

(Received 24 January 2025; accepted 26 June 2025; published 25 August 2025)

Inclusive electron scattering cross sections off a hydrogen target at a beam energy of 10.6 GeV have been measured with data collected from the CLAS12 spectrometer at Jefferson Laboratory. These first absolute cross sections from CLAS12 cover a wide kinematic area in invariant mass W of the final state hadrons from the pion threshold up to 2.5 GeV for each bin in virtual photon four-momentum transfer squared Q^2 from 2.55 to $10.4 \, \text{GeV}^2$ owing to the large scattering angle acceptance of the CLAS12 detector. Comparison of the cross sections with the resonant contributions computed from the CLAS results on the nucleon resonance electroexcitation amplitudes has demonstrated a promising opportunity to extend the information on their Q^2 evolution up to $10 \, \text{GeV}^2$. Together these results from CLAS and CLAS12 offer good prospects for probing the nucleon parton distributions at large fractional parton momenta x for $W < 2.5 \, \text{GeV}$, while covering the range of distances where the transition from the strongly coupled to the perturbative regimes is expected.

DOI: 10.1103/qy4p-dyjt

I. INTRODUCTION

Studies of inclusive electron scattering off protons represent an effective tool for the exploration of the structure of the proton ground state in terms of parton distribution functions (PDFs). The global quantum chromodynamics (QCD)-driven analyses of the experimental results on inclusive electron scattering off nucleons, pp and pd Drell-Yan cross sections, lepton and W boson charge asymmetries, and jet and γ +jet production—with the analyses dominated by the p(e, e')X inclusive data—have provided detailed information on the quark and gluon PDFs in a wide range of fractional parton momenta x from 10^{-4} to above 0.9 and at photon virtualities Q^2 from $\approx 1-10^4 \text{ GeV}^2$ [1–4]. At large x (i.e., x > 0.4 for $Q^2 = 2$ GeV^2 , x > 0.76 for $Q^2 = 10 \text{ GeV}^2$), corresponding to the nucleon resonance excitation region of invariant mass $W \lesssim 2$ GeV, the PDFs have been less explored compared with those at smaller x. The extraction of PDFs from inclusive electron scattering data at large x is faced by constraints imposed by the applicability of the factorization of the perturbative and nonperturbative processes. Isolation of the factorizable contributions requires, beyond accounting for higher-twist effects and target-mass corrections [1,2,5,6], the evaluation of the contributions from nucleon resonance electroexcitations that are clearly seen as peak structures in the W-dependence of the inclusive electron scattering cross sections [7].

Dedicated studies of inclusive electron scattering cross sections off nucleons in the resonance region have been carried out at the Thomas Jefferson National Accelerator Facility [Jefferson Laboratory (JLab)] [8–11]. Measurements of inclusive

electron scattering with the CLAS detector in Hall B [12] have been provided for x up to 0.9 (or W from the pion threshold up to 2.5 GeV) and for Q^2 from 0.25–4.5 GeV² [8]. Because of the large electron scattering angle acceptance of CLAS, the data span the entire kinematically allowed range of W in each given bin of Q^2 with a bin width $\Delta Q^2 = 0.05$ GeV². The inclusive electron scattering experiments in Hall C at JLab [9] extended the Q^2 coverage of the data from $3.6-7.5 \,\mathrm{GeV}^2$ with almost the same range over x (or W) as for the CLAS experiments, while also providing information on the longitudinal and transverse components of the inclusive cross section [10,11]. Because of the small acceptance of the detector in Hall C (\approx 35 mrad for the scattered electron), these p(e, e')X cross sections are available within highly correlated (W, Q^2) values. Therefore, the data from CLAS and Hall C offer complementary information on inclusive electron scattering off protons. The available published data in the deep inelastic scattering regime, W > 2 GeV, were taken at SLAC in the 1980s and span Q^2 up to 9.5 GeV². See Ref. [13] for an

In the analyses of inclusive electron scattering to date, the contribution of excited nucleon (N^*) states has been treated [9,14] within the framework of quark-hadron duality [15,16]. Studies of exclusive πN , ηN , and $\pi^+\pi^-p$ electroproduction off protons with CLAS have provided information on the electroexcitation amplitudes (also known as the $\gamma_v p N^*$ electrocouplings) of most N^* states in the mass range up to 1.8 GeV for $Q^2 < 5$ GeV² [17–22]. Consistent results for the $\gamma_v p N^*$ electrocouplings of the N^* states have

been achieved within independent analyses of the major πN and $\pi^+\pi^-p$ electroproduction channels, demonstrating their reliable extraction [21–25]. This allows for the evaluation of the resonant contributions to the inclusive electron scattering cross sections [26,27] and spin structure functions [28] from the experimental results on the full set of the $\gamma_\nu p N^*$ electrocouplings and their total hadronic decay widths. This paves the way for the first time to gain insight into the ground state nucleon PDFs in the resonance region with N^* parameters taken from the studies of exclusive meson photo-, electro-, and hadroproduction data.

The data with the new CLAS12 detector in Hall B [29] allow for a significant extension of the studies of inclusive electron scattering in the resonance region. In this paper data are presented from the first measurements of inclusive electron scattering off protons using CLAS12 for W < 2.5 GeVand Q^2 from 2.55–10.4 GeV². Owing to the large acceptance of CLAS12, these data further the understanding of the ground state nucleon PDFs as a function of x (or W) over the entire resonance region for W from the pion threshold up to 2.5 GeV in each bin of Q^2 for the first time at $Q^2 > 4$ GeV². The advances in the developments of the novel pseudo- and quasi-PDF concepts [30–32] in connection with lattice QCD [33,34] and advances in continuum QCD approaches [35,36], allow for the computation of the ground state nucleon PDFs in a wide range of x from the QCD Lagrangian. To confront these theory expectations with experimental data in the resonance region it is important to have (a) a reliable evaluation of the resonant contributions from exclusive meson electroproduction data within the framework described in Refs. [26–28] and (b) the measured observables for inclusive electron scattering p(e, e')X with broad coverage over W. The studies at large x in the resonance region are of particular importance for the exploration of strong QCD (referring to the study of phenomena in the regime where the QCD running coupling is large—i.e., comparable with unity), which is responsible for the generation of the ground and excited states of the nucleon from quarks and gluons.

Future analyses of our results at $Q^2 > 4$ GeV² within theoretical approaches with a connection to the QCD Lagrangian [30,31,33–38] will allow the exploration of the evolution of the ground state nucleon PDFs in the resonance region for the first time at distances where the transition from the strongly coupled to the perturbative QCD regimes is expected. Furthermore, the data from CLAS12 will provide new information relevant for studies of quark-hadron duality [9,14] and will shed light on the prospects for the exploration of N^* structure in exclusive electroproduction experiments with CLAS12 [19,25,39,40].

The organization of the remainder of this paper is as follows. Section II provides details on the CLAS12 spectrometer employed for these measurements. Section III provides an overview on the analysis cuts employed to isolate the electron scattering events of interest from the data and Sec. IV discusses the Monte Carlo and event generator. Section V discusses the extraction of the inclusive cross sections and all data correction procedures. Section VI reviews the iterative procedure to improve the event generator model by matching to the data. Section VII describes the statistical uncertainties

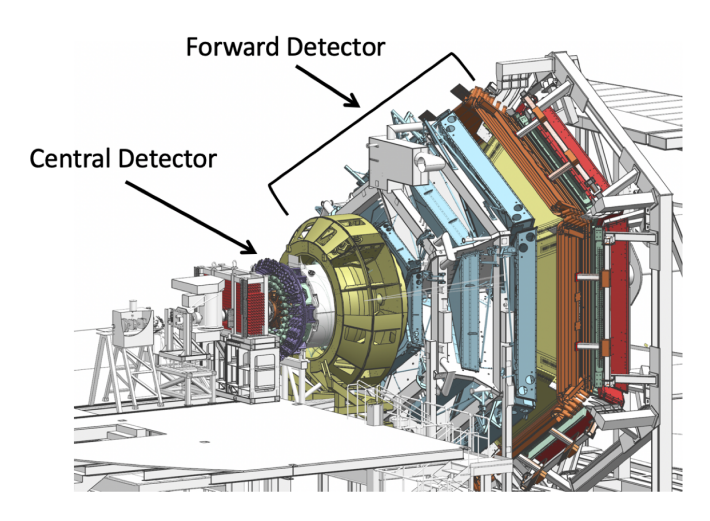


FIG. 1. Model of the CLAS12 detector highlighting the forward detector used for detection of the scattered electron and the central detector about the target. The beam is incident from the left. The CLAS12 detector extends for 13 m along the beamline. See Ref. [29] for details.

and details the different sources of bin-by-bin and scale-type systematic uncertainties in this measurement. Section VIII presents the final cross-section results and discusses their role to offer insight into the evolution of the partonic structure of ground state nucleons at distances where the transition from the strongly coupled to perturbative QCD regimes is expected. Finally, a summary of this work and our conclusions are presented in Sec. IX.

II. CLAS12 DETECTOR

The CEBAF large acceptance spectrometer for operation at 12 GeV beam energy (CLAS12) [29] in Hall B at JLab is used to study electro-induced nuclear and hadronic reactions. CLAS12 was developed as part of the energy-doubling project of JLab's Continuous Electron Beam Accelerator Facility (CEBAF). This spectrometer provides efficient detection of charged and neutral particles over a large fraction of the full solid angle. It is based on a dual-magnet system with a superconducting torus magnet in the forward detector region spanning polar angles from 5° to 35° that provides a largely azimuthal field distribution, and a superconducting solenoid magnet in the central detector region covering polar angles from 35° to 125° with full azimuthal coverage. See Fig. 1 for a model representation of CLAS12.

In the forward direction, the trajectories of charged particles are reconstructed using a multilayer drift chamber (DC) system consisting of 3 sets of detectors called Region 1 (R1), Region 2 (R2), and Region 3 (R3) [41]. Electron identification requires a matching of this track with a signal in the high threshold cherenkov counter (HTCC) [42] close to the target and a cluster reconstructed in the forward electromagnetic sampling calorimeters (ECAL) [43]. Charged particle timing is provided by the forward time-of-flight (FTOF) system [44]. The momentum resolution of the scattered electron is presently at the level of $\Delta p/p \approx 0.5$ –1%. The data acquisition system [45] and detector design allow for operations

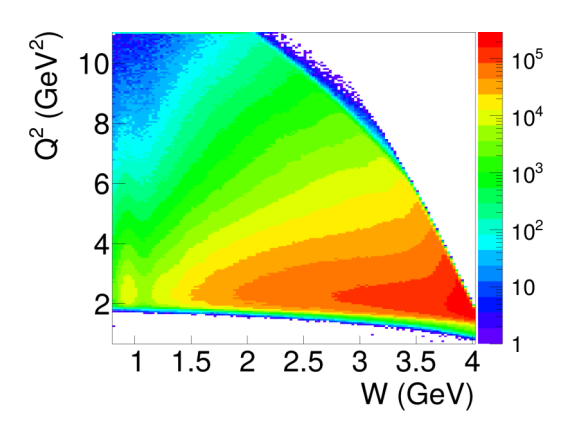


FIG. 2. Data from CLAS12 with a 10.6 GeV electron beam incident on a hydrogen target showing the coverage in Q^2 vs W. For these data the polarity of the torus magnet was set to bend negatively charged particles toward the electron beamline.

at a beam-target luminosity of $1 \times 10^{35} \, \mathrm{cm^{-2} \, s^{-1}}$. The data included in this work were acquired in fall 2018 with a beam energy of 10.604 GeV and a 5-cm-long liquid-hydrogen target. This data collection period was part of CLAS12 Run Group A (RG-A). Typical event rates were 15 kHz and 500 MB/s with a data acquisition livetime above 90%.

The RG-A data acquired in fall 2018 were taken with two detector settings. The first part had an inbending torus field (that bent negatively charged particles toward the beamline) at maximum field strength ($\int Bd\ell$ at nominal full field ranges from 2.8 Tm at 5° to 0.54 Tm at 40°) and the second part had an outbending torus field (that bent negatively charged particles away from the beamline) at maximum field strength. The beam current varied between 45 and 55 nA. The cross-section data presented in this work used only the inbending torus polarity runs to provide the maximal coverage over Q^2 .

Several hardware triggers were defined for the collection of the RG-A fall 2018 inbending data. The specific trigger configuration for this data analysis was defined as

$$DC_{roads} \cdot \cdot HTCC_{nphe} > 2 \cdot \cdot ECAL > 300 \text{ MeV} \cdot \cdot$$

 $PCAL > 60 \text{ MeV} \cdot \cdot (ECin + ECout) > 10 \text{ MeV}.$ (1)

This electron trigger required predefined DC trajectories (called roads) that matched to a cluster in the HTCC with a threshold of two photoelectrons, a minimum deposited energy in the ECAL of 300 MeV, and a minimum energy deposited in specific ECAL sublayers (called PCAL, ECin, ECout) in the same CLAS12 sector [46].

The large forward acceptance of CLAS12 enabled detection of the final-state electron in the inclusive scattering reaction p(e,e')X over a range of W up to 4 GeV and Q^2 from 0.5 to 12 GeV². Figure 2 shows the full kinematic phase space of the scattered electron for these data. With the six coils of the torus magnet, the forward acceptance is divided into six active sectors. Due to the width of the torus coils, the azimuthal acceptance varies with polar angle θ from 50% at 5° to 90% at 35°, which is the maximum polar angle for the final state particles in the laboratory frame covered by the forward detector. The design of the system allows for

TABLE I. EB electron assignment requirements. The ECAL sampling fraction used by the EB is parameterized as a function of the total energy deposited in the ECAL. Note that the ECAL is subdivided into three module stacks, PCAL, ECin, and ECout [43].

Cut	Limits
Electric charge	Negative
Number of photoelectrons	$N_{\mathrm{phe}} > 2$
Min. PCAL energy	$PCAL_{dep} > 60 \text{ MeV}$
Sampling fraction vs E_{dep}	±5σ

six independent measurements that are ultimately combined to present the final measured cross sections. However, each separate measurement allows for cross checks of the assigned systematic uncertainties.

III. ANALYSIS CUT OVERVIEW

A series of criteria, or cuts, was applied to the multiple detector responses to identify negatively charged tracks that are electron candidates. The cuts were designed to discriminate against minimum-ionizing particles (MIPs), such as negative pion (π^-) tracks. The CLAS12 event builder (EB) [47] protocol first assigns electron identification to tracks with responses in the HTCC and ECAL that satisfy the criteria in Table I, with an associated geometrically matched hit in FTOF. After the EB identifies electron candidates, additional cuts were applied to the data to select a refined sample of candidate electrons prior to proceeding with the remainder of the analysis.

The electric charge of a candidate particle will dictate its curvature as it traverses through the toroidal magnetic field. The field will deflect particles along the polar angle, either making their curvature "inbending" or "outbending" based on the field polarity. Reconstruction algorithms take the track curvature into account to assign a charge. Since electrons need to be identified, only negatively charged tracks were selected. Electrons in CLAS12 can only be identified in the forward detector. The HTCC aids in reducing negative pion contamination in the electron sample for candidate tracks up to 4.9 GeV (the threshold for π^- to begin generating an HTCC signal in the CO₂ radiator gas), based on reading out photomultiplier tubes (PMTs) to determine the number of photons emitted via Cherenkov radiation by a charged track traversing the detector volume. Up to the π^- momentum threshold it is sufficient to cut on the number of photoelectrons $(N_{\rm phe})$ produced in the detector. An electron candidate track will typically produce more than two photoelectrons (the CLAS12 trigger threshold), which is the minimum threshold for this cut. This cut is automatically enforced when using the EB particle identification assignment to select electrons in the forward detector. Beyond the HTCC efficiency corrections detailed in Sec. V A 2, no HTCC fiducial cuts were applied, since the HTCC provides only a crude and discrete hit distribution from its PMT information.

The target in the experiment was a 5-cm-long cell filled with liquid-hydrogen. Using tracking information from the drift chambers projecting back to the e+p interaction point, a cut on the reconstructed vertex coordinate along the beamline

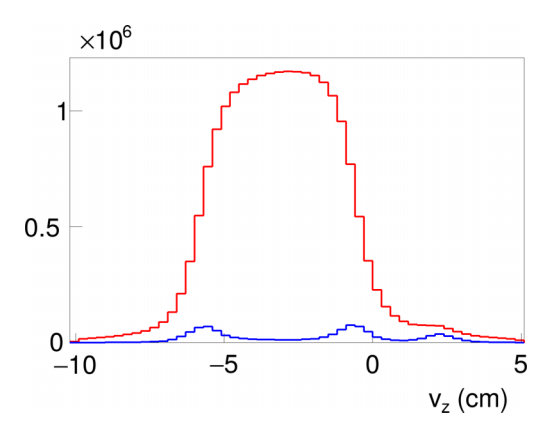


FIG. 3. Vertex coordinate distributions (v_z) for full target runs (red) and for empty target runs (blue) normalized by charge for a single CLAS12 sector. The small bump at $v_z \sim 2$ cm is from the target cell heat shield.

(labeled as the z axis of CLAS12) was applied to ensure the event originated from the target location. A cut on the vertex z coordinate from (-8.0, 2.0) cm was applied to account for the ≈ 1 cm drift chamber trace-back resolution. Figure 3 illustrates the v_z distributions for a single CLAS12 sector for the full (red) and empty (blue) target data.

Drift chamber fiducial boundary cuts were applied based on the reconstructed hit coordinates to select charged tracks that were detected in regions where the detector efficiency was high and uniform. The cuts were placed within a small distance from the detector borders to make sure that only tracks in the fiducial volume were selected for analysis. The cuts are sector independent and depend only on the layer (i.e., the R1, R2, and R3 drift chambers). A similar fiducial cut in the PCAL plane was also applied to remove events outside of the fiducial volume between the DC and PCAL. The cut was based on the PCAL scintillation strip coordinate information along the three sides of the triangular module geometries.

An ECAL sampling fraction cut was applied to remove non-minimum-ionizing pion tracks. The sampling fraction is defined as the ratio of the total energy deposited in all layers of the ECAL to the reconstructed momentum, P, of the track determined from the drift chambers. The sampling fraction signature for electrons is nearly constant at a value of ~ 0.25 across all momenta. This implies the deposited energy scales with the momentum or deposited energy of the electron. The electron tracks are selected with a 3.5σ cut below the parameterized sampling fraction (no upper cut is necessary) as a function of the deposited energy E_{dep} as seen in Fig. 4. The cut, which was designed to be tighter than that employed by the EB, was developed by fitting the sampling fraction for successive bins in deposited energy. A Gaussian function was fit to determine the mean μ_b and sigma σ_b for each bin b. A polynomial was fit to the mean and sigma to create an energydependent sampling fraction cut for each CLAS12 sector. The parameters are the result of fits to the sampling fraction distribution in bins of deposited energy, separately, for each sector in data and a sector-independent fit in simulation.

Sometimes pions can be identified as electrons, especially for higher momentum tracks. To further reduce the pion

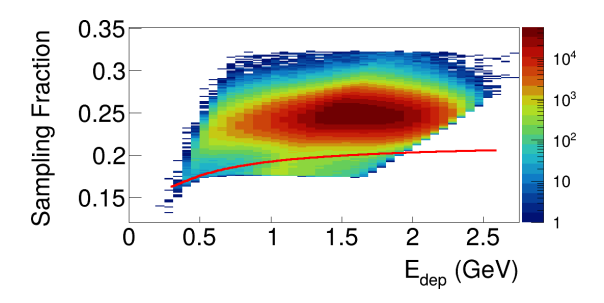


FIG. 4. ECAL sampling fraction as a function of deposited energy in all layers for a single sector. The red line is the 3.5σ cut. Here kinematic cuts from 0.8 < W < 2.7 GeV and $2.18 < Q^2 < 10.6$ GeV² were applied.

contamination, the correlation of the sampling fractions calculated separately from the PCAL and ECin was studied. A linear cut in the sampling fraction plane was introduced based on simulation studies to reduce the leakage of pions into the electron sample (see Fig. 5). This cut is referred to as the partial sampling fraction cut.

Inaccuracies in the magnetic field map and unaccounted detector misalignments resulted in systematic misreconstruction of the momentum for charged particles. These effects in turn result in misreconstruction of Q^2 and W for the events. A correction was developed as a function of P, θ , and ϕ for the electron detected in each of the six sectors of the CLAS12 forward detector to minimize such deviations. These corrections were below the level of 0.5%. A detailed discussion of the applied momentum correction method can be found in Ref. [48].

IV. MONTE CARLO

A. GEMC—Geant4 Monte Carlo

The CLAS12 detector simulation has been implemented within the GEMC software framework [49]. GEMC is used to accurately calculate the CLAS12 acceptance, including the detector response, geometrical acceptance, and charged particle tracking efficiency. GEMC is a C++ framework that uses Geant4 [50] to simulate the passage of particles through matter. Particles are transported through the detector materials and produce radiation, hits, and secondaries. GEMC then

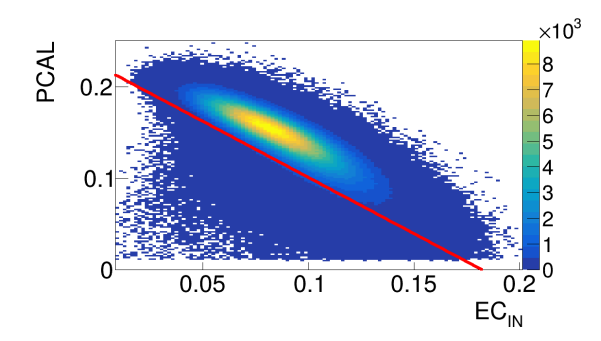


FIG. 5. Sampling fractions from PCAL vs ECin for a single sector for a representative momentum bin (6 < P < 7 GeV). The partial sampling fraction cut employed is shown by the red line.

collects the Geant4 results and produces the digitized output in the same data format as that from the detector. All of the elements within the particle trajectory paths to any of the CLAS12 detectors are included in the simulation. In addition, the simulation has been tuned to reproduce beam-related background hits in the detectors to a good level of accuracy to properly model charged particle tracking efficiencies. The simulations performed for this analysis employed the same version of the reconstruction code as was used for data processing.

B. Event generator

The event generator (EG) developed by Sargsyan used for the inclusive electron scattering Monte Carlo (MC) was based on the Bodek parameterization of the world data [51]. It describes both the elastic and inelastic parts of inclusive electron scattering and allows for these parts to be switched on or off for the purpose of event generation. Radiative effects were accounted for using the Mo and Tsai approach [52] for both the elastic and inelastic parts of the cross section. Note that the code also has the option to turn these effects on or off, which was used to account for internal radiative corrections in the p(e, e')X cross-section extraction from the measured data. The EG code was designed to account for external radiation in the target cell and target material before the e + p interaction point. While the momentum loss associated with radiative effects for the incoming and scattered electrons was taken into account, the radiative photon itself was not generated, and only the scattered electron was available in the final state. The external radiation after the e + p interaction point was accounted for by GEMC.

The simulations were carried out accounting for all non-functioning detector elements that were seen in the data, including holes in the drift chambers due to broken wires or bad readout boards and missing channels in the ECAL and FTOF. In this way the geometrical acceptance of the MC was matched closely to the data. The simulations used the same code as was used for analysis of the data. To ensure that the ultimate EG model was realistic and did not introduce significant bias in the measurements, the original EG was tuned to match the extracted cross sections as discussed in Sec. VI.

C. Background merging

The simulations for this analysis employed a background merging option to best match the backgrounds in the various CLAS12 detector subsystems [53]. Of relevance for this analysis is the hit merging for the DC, FTOF, and ECAL systems. This background was developed based on CLAS12 data collected with a random trigger at the production beam current that was merged with the MC event-by-event. As the background was determined based on actual data from CLAS12 taken in the exact same conditions as the data used for analysis, it matches well the overall background distribution in the detector. This includes the local DC hit occupancy necessary to properly model the tracking efficiency across the full forward detector acceptance at the different beam currents used for production data collection in this experiment. Merg-

ing of background events with simulation was performed at the level of raw ADC and TDC hits. The background merging procedure is essential to match the charged track reconstruction efficiency from simulation to the efficiency measured with data. A comparison of the tracking efficiency from MC at the beam current used for data collection is shown in Sec. V A 3.

D. Monte Carlo smearing

Studies of the missing mass distributions from exclusive meson electroproduction show that the CLAS12 MC used for this analysis gives a better momentum resolution for charged tracks than is seen in the data by a factor of 1.5–2. The GEMC reconstruction includes two primary deviations from the generated (true) momentum values

- (1) ΔP^{res} —deviation based on momentum resolution, which is centered around zero,
- (2) ΔP^{loss} —deviation based on physical energy losses (e.g., radiative effects) or detector imperfections, which is typically not centered around zero.

Our goal was to smear the GEMC momentum resolution (ΔP^{res}) without amplifying or altering any legitimate physical effects (ΔP^{loss}). To parametrize the GEMC resolution model as a function of the kinematic variables, a simulation sample of $ep \rightarrow e'\pi^+ n$ events was generated with the AAO GEN EG [54]. The simulation was performed in the same W and Q^2 range used in our inclusive measurement. The simulation sample was split into a kinematic grid in polar angle θ and the distributions of $(P^{\text{gen}} - P^{\text{rec}})/P^{\text{rec}}$ were fit for the e' and π^+ for each cell of the grid. The extracted widths were given by $\sigma^{\text{GEMC}}(\theta_{\sigma})$, where g is the grid cell identifier. Considering that only a narrow range of momentum was associated with each θ bin, the resolution did not show significant momentum dependence across a given cell. With this procedure the resolution for both the e' and π^+ was obtained as a function of θ . To compare the resolution in the data with that determined from the MC, we calculated $\delta P/P$ for both particles from data and simulation, where δP is the difference between the calculated or generated momentum and the reconstructed momentum. The calculated momentum for the electron from data was obtained from the electron polar angle and the pion four-momentum and similarly for the pion. The electron momentum smearing for the inclusive analysis was based on using

$$P^{\text{new}} = P^{\text{rec}} + P^{\text{rec}} \sigma^{\text{GEMC}}(\theta) \text{ gaus}(0, 1) F(\theta),$$
 (2)

where $P^{\rm rec}$ and $P^{\rm new}$ are the electron momentum before and after smearing, respectively, $\sigma^{\rm GEMC}(\theta)$ is the resolution function, F is the determined smearing factor, and gaus(mean, sigma) represents a random number sampled from a Gaussian distribution with the given mean and width.

Starting with F=1.0 (an arbitrary value), F was increased separately for all kinematic bins until good agreement (matching $\delta P/P$ for data and simulation) was achieved. The comparisons with the final functional $F(\theta)$ with resolution nearly twice worse than the original MC gave reasonable agreement (at the level of 10%) of the reconstructed momenta between data and simulation as shown in Fig. 6.

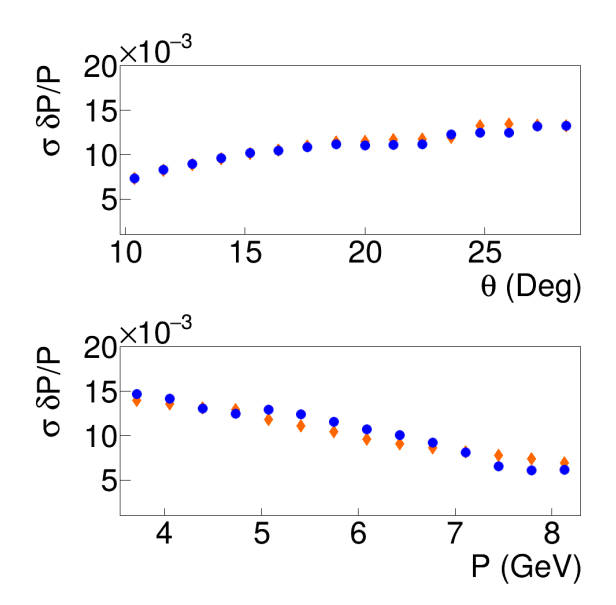


FIG. 6. $\delta P/P$ vs θ and P, where $\delta P/P$ represents $(P^{\text{calc/gen}} - P^{\text{rec}})/P^{\text{rec}}$, for electrons from data (blue) and simulation (orange) with smearing.

For the inclusive scattering case, we applied the smearing factor (F) obtained from the exclusive reaction study. The MC momentum smearing aligns the W spectra quite well as shown in Fig. 7. Finally, a realistic average resolution function was estimated for the CLAS12 data as a function of W using our smearing procedure. Figure 8 shows the width σ of $W_{\rm gen}-W_{\rm rec}$ as a function of W for our lowest and highest Q^2 bin values.

E. Comparison of MC to data

For the purpose of a direct comparison of our MC and the data, both the elastic and inelastic parts were invoked in the MC, as well as full radiative effects in the EG. Here the

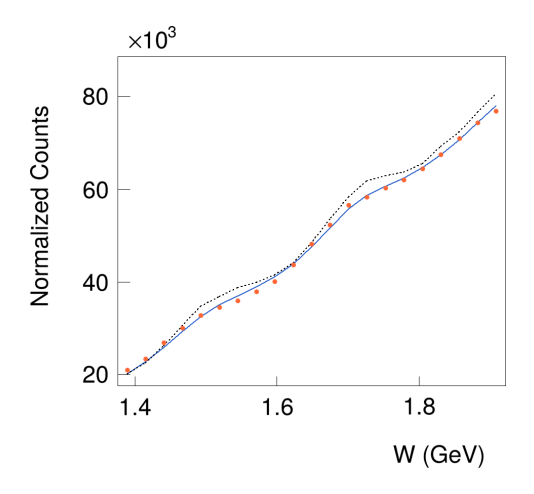


FIG. 7. W spectra for a representative Q^2 bin $(4.08 < Q^2 < 4.78 \, \text{GeV}^2)$ for data (orange points), MC without smearing (black dashed line), and MC with the applied smearing function (blue line). The resolution smearing procedure matches the MC distributions to the data.

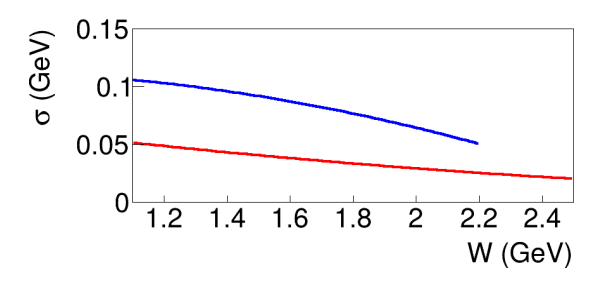


FIG. 8. Resolution vs W from MC applying smearing for the reconstructed p(e, e')X events within the bin of minimal Q^2 from 2.55–2.99 GeV² (red) and maximal Q^2 from 8.94–10.4 GeV² (blue).

final version of the EG was used that was obtained after the adjustment procedure described in Sec. VI A. The simulation was normalized to the data luminosity by the factor

$$\frac{\int \mathcal{L}dt \,\sigma_{\text{EG}}}{N_{\text{total}}},\tag{3}$$

where

- (1) $\int \mathcal{L}dt$ is the integrated luminosity given by the product of the number of incident beam electrons and the number of target particles per area,
- (2) σ_{EG} is the integrated cross section obtained from the EG for the generated kinematic region, and
- (3) N_{total} is total number of generated events.

Figure 9 shows comparisons between the measured data and reconstructed simulation for a single representative CLAS12 sector for the momentum, polar angle, Q^2 , and azimuthal angle distributions. Dips in the polar angle distributions correspond to knocked out elements in the ECAL or other CLAS12 forward detector subsystem elements. Overall the distributions show very close agreement between the data and the simulation model.

V. CROSS-SECTION EXTRACTION

The following expression was used to compute the differential cross section in each kinematic bin i:

$$\frac{d\sigma_i}{dQ^2dW} = \frac{1}{(\Delta Q^2 \Delta W)} \frac{N_i}{\eta_i N_0 R_i BC_i} \frac{CMB}{(N_A \rho t / A_w)}.$$
 (4)

The terms in this expression are defined as

- (1) $\Delta Q^2 \Delta W$: kinematic bin volume
- (2) N_i : number of reconstructed electrons in each bin that pass our cuts
- (3) η_i : acceptance and efficiency correction
- (4) N_0 : number of incident beam electrons
- (5) R_i : radiative correction
- (6) BC_i : bin-centering correction
- (7) $N_A \rho t/A_w$: target number density with N_A Avogadro's number, ρ the liquid-hydrogen density (0.07151 g/cm³), t the target length, and A_w the atomic weight of hydrogen (1.00794 g/mol)
- (8) CMB : cm² to μ b conversion factor of 1 × 10³⁰.

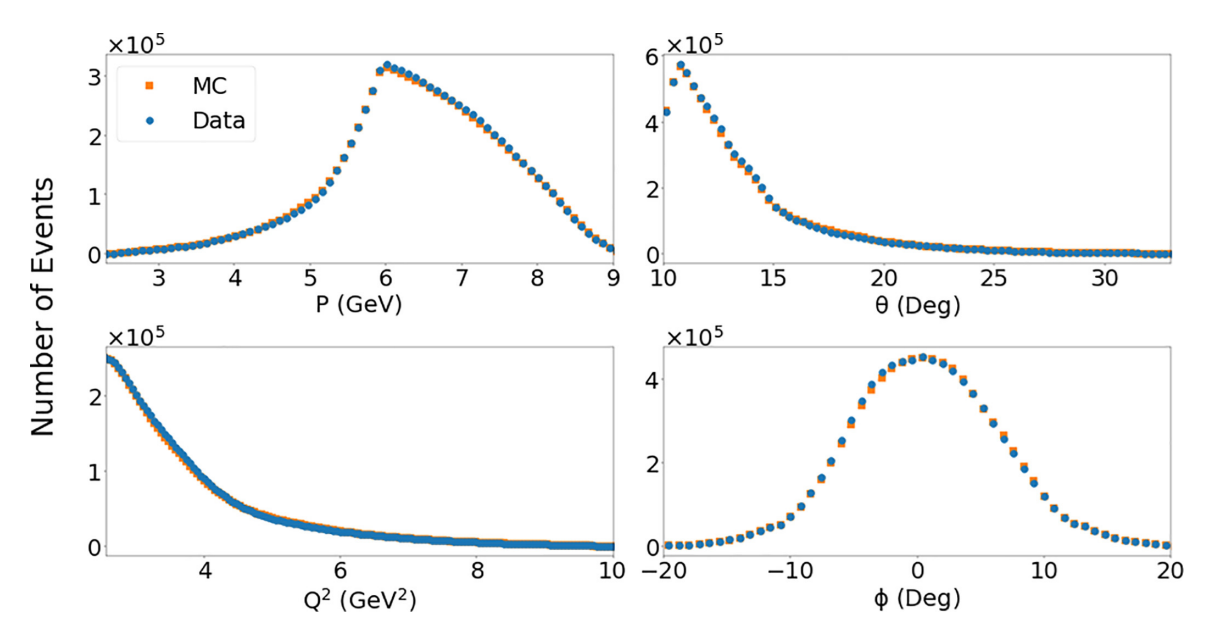


FIG. 9. Comparison of the measured (blue) to reconstructed MC event distributions (orange) for a single representative CLAS12 sector for (UL) momentum, (UR) polar angle θ , (LL) Q^2 , and (LR) azimuthal angle ϕ . The MC distributions were normalized to the data by the luminosity factor of Eq. (3).

A. Electron events

1. Empty target subtraction

In the event distribution, there is a contribution that comes from the 30-µm-thick aluminum end-caps of the cryotarget cell. This contribution is not related with inclusive electron scattering off hydrogen, so it must be removed. Our dataset contains special runs that were collected with an almost empty target (i.e., only residual cold hydrogen gas in the target cell). The events obtained from these runs were used for the subtraction of the empty target contribution. We extracted events from the empty target runs with exactly the same electron requirements and cuts as were used for the full target runs. However, we put an additional cut on v_z , namely, we removed the middle part of the target cell from $-4.7 < v_z < -1.65$ cm to minimize the over-correction for the residual hydrogen gas in the target cell. The empty and full target runs have different Faraday cup charges (the full target runs had \sim 12 times more charge), so the empty target events were properly normalized. The events after the empty target contribution subtraction are given by

$$N_{\text{hydrogen}} = N_{\text{full}} - N_{\text{empty}} \frac{Q_{\text{full}}}{Q_{\text{empty}}},$$
 (5)

where $N_{\rm hydrogen}$, $N_{\rm full}$, and $N_{\rm empty}$ are the events for inclusive events from hydrogen, the full target cell, and the empty target cell, respectively, and $Q_{\rm full}$ and $Q_{\rm empty}$ are the corresponding Faraday cup charges for the full target and empty target runs. Note that this approach does not take into account the small tracking efficiency difference between the full and empty target data.

2. Cherenkov counter efficiency correction

We looked at the HTCC photoelectron response in bins of x and y, where x and y are the coordinates of intersection of

the track with the mirror in the laboratory frame. For every bin the photoelectron spectrum was fit with a Poisson distribution. The ratio of the Poisson distribution integrals obtained for the number of photoelectrons in the range from [2,50] to [0,50] was used to determine the HTCC efficiency map for each (x, y) bin that accounted for the efficiency loss due to the two photoelectron requirement in the trigger and the EB. The procedure was applied to both the data and MC.

The difference between the HTCC efficiency from data and simulation is attributed to nonuniformities in the mirror surface (both in terms of reflectance and geometry), which results in signal dispersion and nonoptimal overlap with the acceptance of the HTCC PMTs (which themselves could be slightly misaligned). To obtain the correction factor for every (x, y) bin, we took the ratio of efficiencies for data to MC. The final HTCC efficiency map that was used in the analysis is shown in Fig. 10. The map contains efficiency corrections for all x and y bins in the range (-125, 125) cm, with a bin size of 1 cm. To correct for the HTCC inefficiency, a weight of $1/\epsilon$, where ϵ is the efficiency from the map, was applied to the reconstructed events.

3. Forward tracking efficiency

As the beam current increases, the forward tracking efficiency decreases. The analysis of the tracking efficiency from data was completed using data taken from a luminosity scan analysis as shown in Fig. 11. The inefficiency increases linearly with increasing beam current with a slope of -0.41%/nA. This inefficiency factor is accounted for in combining the data in this analysis taken at different beam currents from 45–55 nA. After applying the efficiency correction factor to our dataset, we see good agreement between the cross sections determined using the 55 and 45 nA data runs using only a 45 nA simulation sample. The blue star

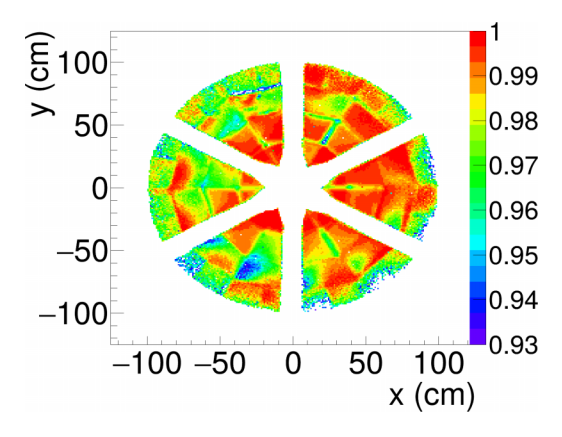


FIG. 10. Efficiency correction map for the HTCC over the y vs x coordinate acceptance of the detector. Sector 1 is located at x > 0 and centered around y = 0. The sector number increases counterclockwise. Note the truncated z scale for the efficiency.

at 45 nA in Fig. 11 is the tracking efficiency estimated from MC. It is seen to agree with the data measurement within the assigned uncertainties. The systematic uncertainty assigned to the efficiency is discussed in Sec. VII B.

This correction was applied directly to the Faraday cup charge using

$$C_{\text{eff}} = 1 - 0.0041 (I_{\text{run}} - 45),$$

 $Q_{\text{corr}} = Q_{\text{run}} C_{\text{eff}},$ (6)

where $I_{\rm run}$ is the nominal beam current in nA for a given run, $Q_{\rm corr}$ the Faraday cup charge in nC after correction for the detector efficiency loss, $Q_{\rm run}$ the Faraday cup charge in nC, and $C_{\rm eff}$ is the correction factor that depends on beam current. $Q_{\rm corr}$ was used for the integrated experiment electron current. Strictly speaking, this correction accounts for the

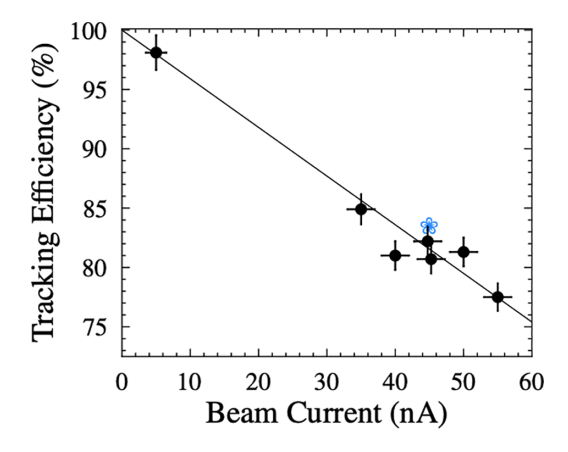


FIG. 11. Efficiency vs beam current for negatively charged particles in the CLAS12 forward detector from luminosity scan data (black data points) using the reconstruction software version employed for this analysis. The black line shows a linear fit with a slope of -0.41%/nA. The vertical error bars represent the systematic uncertainty in the measurement and the horizontal error bars represent the spread in beam currents associated with the data points. The blue star at 45 nA is the tracking efficiency determined from the MC with appropriate background merging.

decrease of the forward tracking efficiency at the higher beam current (i.e., higher luminosity) that affects the reconstructed inclusive events. Our approach to account for this by applying the correction to the Faraday cup charge amounts to the same thing but was done in this way as a convenience in the data analysis.

B. Data binning

The CEBAF 10.6 GeV electron beam, combined with the broad polar and azimuthal angle acceptance of CLAS12, provides a wide kinematic range over both W and Q^2 , with the ability to cover the full resonance range in W for any given Q^2 . This feature is especially important for studies of inclusive electron scattering in the resonance region of $W \lesssim 2$ GeV. The peaks seen in the first, second, and third resonance regions (at $W \approx 1.2$ GeV, ≈ 1.5 GeV, and ≈ 1.7 GeV) make application of interpolation procedures over W and Q^2 rather questionable. The validation by the p(e,e')X cross sections measured within a broad W-range in any given Q^2 bin is definitely needed.

Accounting for the nucleon resonance contributions in inclusive electron scattering also dictates the desired binning over W, as we want to map out the structures in the W spectrum with as fine detail as possible. However, the finite resolution of the CLAS12 detector sets a lower bound on the practical size of the W bins. A reasonable compromise is achieved with a W bin width of 50 MeV for the covered W range from 1.125 to 2.525 GeV. As detailed in Fig. 8 where the CLAS12 W resolution is shown, the chosen W bin width is consistent with the average detector resolution.

The prominent feature of inclusive electron scattering, namely its fast drop-off with increasing Q^2 , prevents us from using uniform binning. Hence, we chose to employ a logarithmic binning over Q^2 . To define the Q^2 bins, we selected the Q^2 range from $Q^2_{\min} = 2.557 \,\text{GeV}^2$ to $Q^2_{\max} = 10.456 \,\text{GeV}^2$ in $N_Q = 9$ bins as described in Eq. (7). The last line in Eq. (7) gives the bin number as a function of Q^2 :

$$Q_{\min}^{2} = 2.557 \text{ GeV}^{2},$$

$$Q_{\max}^{2} = 10.456 \text{ GeV}^{2},$$

$$N_{Q} = 9,$$

$$\Delta Q^{2} = \log (Q_{\max}^{2}/Q_{\min}^{2})/N_{Q},$$

$$bin(Q^{2}) = \log (Q^{2}/Q_{\min}^{2})/\Delta Q^{2}.$$
(7)

The Q^2 -dependence of the reconstructed electrons shows a strong acceptance-related fall-off at $Q^2 < 2.5 \text{ GeV}^2$. Therefore, we started our analysis at $Q^2 = 2.55 \text{ GeV}^2$ to stay in the area where we have well-defined control over the electron detection efficiency. We have nine bins over Q^2 in the range from $2.55-10.4 \text{ GeV}^2$. For W, we started at 1.15 GeV (which is the center of the lowest bin, so the minimum W is 1.125 GeV), which is close to the inelastic threshold value (1.08 GeV). The cross section is small at low W, so we were limited by statistics and did not go lower. The focus of this analysis is the resonance region, so the last W bin center was set to W = 2.5 GeV for all but the last Q^2 bin. In the last Q^2 bin we had to stop at W = 2.25 GeV because of the detector acceptance.

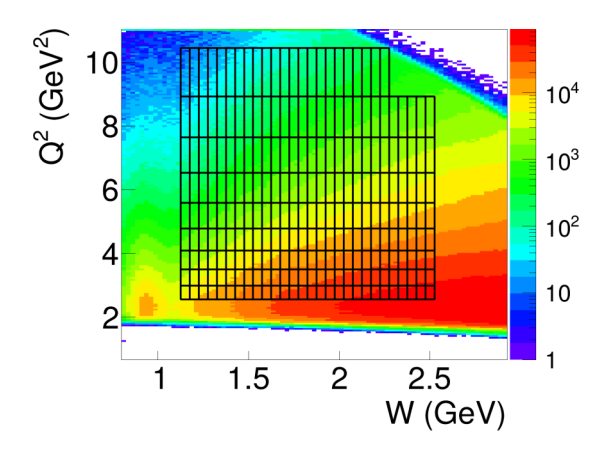


FIG. 12. Q^2 vs W distribution for the inclusive electrons for the RG-A fall 2018 inbending dataset. The black lines show the kinematic binning used for this cross-section analysis in the nucleon resonance region.

The Q^2 vs W phase space of the RG-A fall 2018 inbending dataset used for this analysis is shown in Fig. 12 overlaid with the chosen binning grid.

C. Data unfolding procedure

To mitigate the problem of bin migration (the misidentification of a kinematic bin due to effects of finite resolution, acceptance, and distortions, among others), we employed our MC with its response function matching the data. The bin migration can be accommodated by a matrix $R_{i,j}$ transformation

$$x_i = \sum_{j=0}^{n} R_{i,j} y_j,$$
 (8)

where y represents the "true" distribution and x represents what is reconstructed. The response function $R_{i,j}$ is the probability for an inclusive p(e, e')X event generated in bin j to be reconstructed in bin i. It can be obtained from simulation as the number of events generated in bin j but reconstructed in bin i divided by the total number of generated events in bin j. In our analysis the bins i and j represent (W, O^2) bins.

The acceptance matrix is shown for the one-dimensional (1D) and two-dimensional (2D) cases in Fig. 13. In our nominal analysis we account for 2D (W, Q^2) bin migration effects.

The deconvoluted distributions y_i can be obtained by

$$y_j = R_{i,j}^{-1} x_i. (9)$$

Even if $R_{i,j}^{-1}$ is well defined, it can cause large variations in the deconvoluted distributions, so it is crucial to find a way to come up with a reasonable and applicable $R_{i,j}^{-1}$. A detailed explanation of the theory and formalism behind practical unfolding methods can be found in Ref. [55]. In the remainder of this subsection, the two different deconvolution approaches considered for this work are discussed along with a comparison of the methods.

1. Bin-by-bin method

The most common method to estimate R^{-1} is the bin-bybin method. In the 1D case, the relevant matrix is given by R_i , the ratio of reconstructed events in bin i relative to the number of generated events in bin i:

$$y_i = \frac{N_{\text{rec}_i}}{N_{\text{gen}_i}} x_i. \tag{10}$$

This method does not track the probability for an event generated in bin i to be reconstructed in a different bin j, and its ability to account for event migration between different bins of (W, Q^2) depends directly on the quality of the event generator and the detector simulation. The simulation provides the matrix R^{-1} , so consequently this method is free from uncertainties related to the matrix inversion mentioned above.

2. Richardson-Lucy (iterative bayes) deconvolution

Deconvolution methods employ the matrix R determined from simulation evaluated according to Eq. (8). The deconvoluted distributions can be evaluated from Eq. (9) using the inverse matrix R^{-1} . In our studies, we used the Richardson-Lucy or iterative bayes deconvolution method. A detailed description of this method is available in Ref. [56]. Using the same notation as above, with the true distribution $y = y(y_1, \ldots, y_n)$ and the measured distribution $x = x(x_1, \ldots, x_n)$,

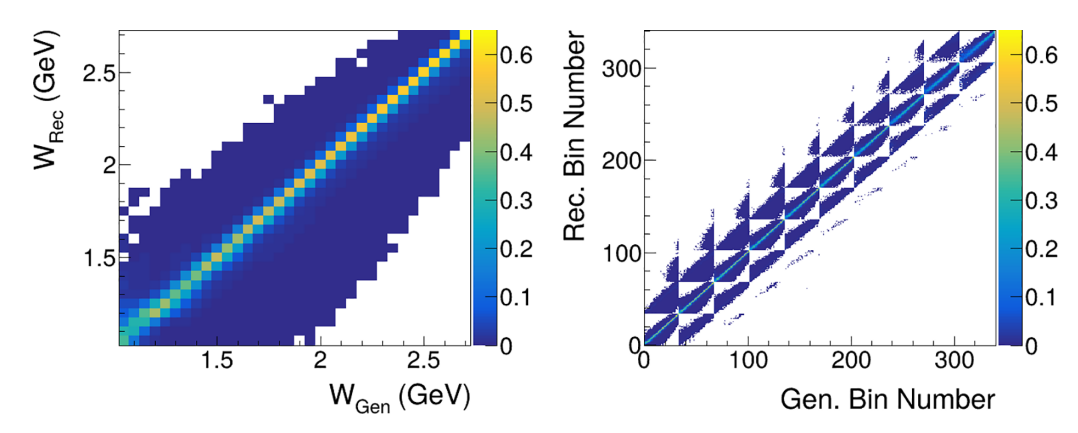


FIG. 13. Acceptance matrix of bin migration for the 1D case (left) in terms of the reconstructed W_{rec} distributions for the generated events in the W_{gen} bins summed over all Q^2 bins and the 2D case (right) where each rectangular panel shows similar distributions as for the 1D case but in the different (W, Q^2) intervals. Each primary group is binned in W, with the x and y axes labeling the 2D-group bin numbers.

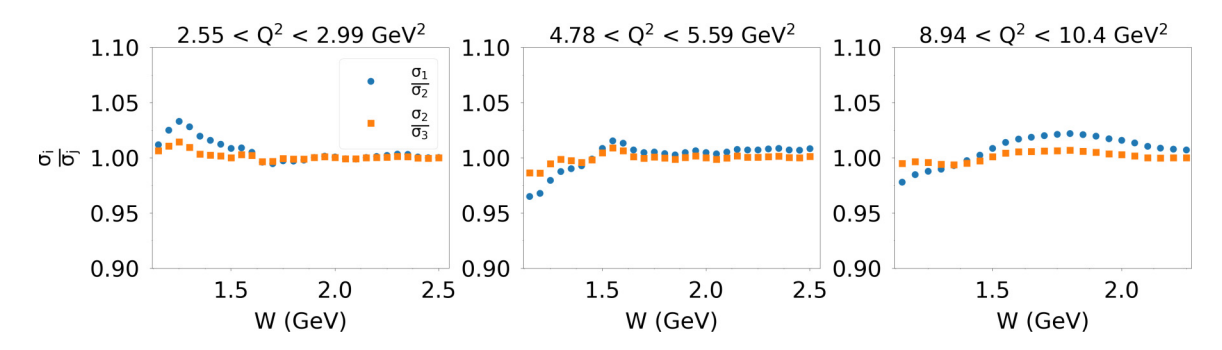


FIG. 14. Ratio of deconvoluted cross sections with the 2D Iterative Bayes algorithm for iteration i = 1 to j = 2 (blue) and for i = 2 to j = 3 (orange) for 3 representative Q^2 bins.

then

$$y_i = \frac{1}{\epsilon_i} \sum_{i=0}^n x_j P(y_i | x_j), \tag{11}$$

where $P(y_i|x_j)$ is the probability of an event reconstructed in bin j to be generated in bin i:

$$P(y_i|x_j) = \frac{P(x_j|y_i)P(y_i)}{\sum_{l=0}^{n} P(x_j|y_l)P(y_l)}.$$
 (12)

There is a chance that some events are not reconstructed at all, so an efficiency ϵ_i was introduced, which is

$$\epsilon_i = \sum_{i=0}^n P(x_j | y_i). \tag{13}$$

All of the probabilities can be determined from MC. After deconvolution $P(y_i)$ can be re-estimated, which is our new best estimate (better than the generated distribution estimate):

$$P_1(y_i) = \frac{y_i}{\sum_{i=0}^n y_i}.$$
 (14)

Using this new $P_1(y_i)$, we can start over and perform a second deconvolution iteration.

This procedure was applied separately to each sector. We constructed response matrices for each sector, estimated events, and performed the deconvolution procedure. Figure 14 shows comparisons for three iterations. Even after two iterations, the events for all Q^2 bins converged and did not change

with iteration number. Therefore we used two iterations in our deconvolution procedure.

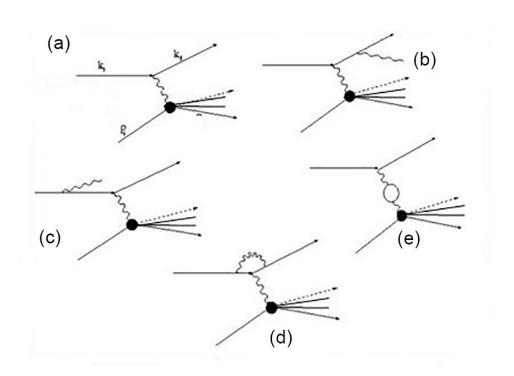
3. Method comparison

As discussed above, we considered two different unfolding methods in the cross-section extraction (bin-by-bin and Bayesian) to account for bin migration effects. The deconvolution for the Bayesian method was done using the RooUnfold package [57]. The bin-by-bin method was implemented using the definition from Sec. VC1. For the Bayesian deconvolution, we filled response matrices for each sector.

To properly account for event migration, the simulation should be performed within the same or an even broader area over W and Q^2 than for the region populated by the measured events. We deconvoluted the extracted events in the W range from 0.825 to 2.825 GeV and Q^2 from 2.18 to 12.0 GeV 2 . The bin-by-bin and Bayesian deconvolution methods were seen to give consistent results for all W and Q^2 bins, with variations of only a few percent. Our final choice of unfolding method for this analysis was the Bayesian method.

D. Radiative corrections

Radiative effects are present in both inclusive and elastic electron scattering as shown in Fig. 15. Our inclusive EG incorporated internal radiative effects based on the Mo and Tsai [52] approach with the option to run with them "on" or "off." This feature allowed us to conveniently evaluate radiative corrections by calculating the cross section with and



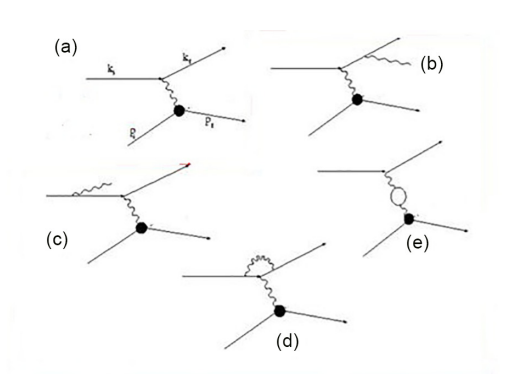


FIG. 15. Feynman diagrams contributing to the Born amplitude and the radiative effects for inclusive electron scattering (left) and elastic scattering (right): (a) Born amplitude, (b), (c) internal bremsstrahlung, (d) vertex correction, and (e) vacuum polarization.

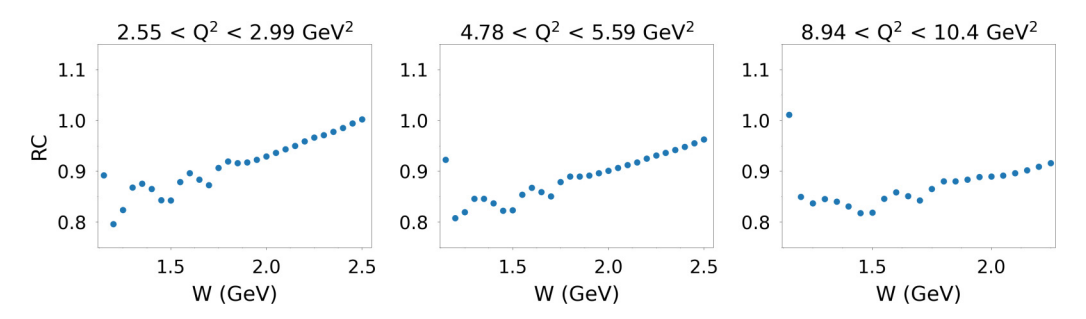


FIG. 16. Radiative corrections (RC) vs W for 3 representative Q^2 bins calculated as the ratio of the radiative to nonradiative cross sections.

without radiative effects for each W and Q^2 bin for which we report our results. As noted in Sec. IV, our radiative model described both the elastic and inelastic parts of inclusive electron scattering. The final version of the EG that we obtained after the adjustment procedure described in Sec. VIA was used. We divided every W and Q^2 bin into 11 subbins in W and 21 subbins in Q^2 (these subbins were uniform in both W and Q^2). There are 231 bins in total for each W and Q^2 bin (11×21) . The reason for smaller binning in Q^2 is due to the fact that we used wide bins in Q^2 and narrow bins in W. We calculated the cross section with and without radiative effects in the center of each subbin. Using the cross-section values in each smaller bin i, we calculated the average cross section over the entire W and Q^2 bin. The radiative correction factor R was computed as the ratio of the radiative to nonradiative cross sections as

$$R(W, Q^2) = \frac{\sum_{i=1}^{231} \sigma_{RC_i}(W_i, Q_i^2)}{\sum_{i=1}^{231} \sigma_{noRC_i}(W_i, Q_i^2)}.$$
 (15)

Figure 16 shows the results of the radiative correction calculation procedure. Note that all external radiation effects after the e+p interaction point are modeled within GEMC and accounted for by our analysis cuts and unfolding procedures.

E. Bin-centering corrections

When calculating the cross section, one actually obtains an average value within the 2D (W, Q^2) bin. Assigning this value to the center point of the bin is justified in the case of a linear dependence across the bin, although in more realistic situations, this is not the case.

A procedure was developed to calculate a correction that takes this effect into account. By dividing each of our 28×9 twofold (W, Q^2) bins into 11 by 21 subbins (for a total of

 \approx 60 000 bins), the cross section was calculated in each subbin using the EG. The computed cross sections were then averaged to obtain the bin-centering correction defined by

$$BC(W, Q^2) = \frac{\sum_{i=1}^{231} \sigma_i(W_i, Q_i^2)}{\sigma_{center}(W, Q^2) \, 231}.$$
 (16)

Figure 17 illustrates the results of the bin-centering correction calculation procedure. The structures in the corrections as a function of W correspond to the resonance peaks in the second and third resonance regions where the central point of the bin is located at the maxima and then the ratio in Eq. (16) decreases due to the maxima in the denominator. There are no structures in the Q^2 evolution of the cross sections so it does not introduce any other structures in our correction factor. Table II details the Q^2 bin limits for the nine bins used in this analysis and provides the bin-centered Q^2 value for each bin. Note that the subplots in the following figures are labeled with the Q^2 bin limits instead of the geometric center bin values.

VI. ITERATIONS

Having discussed all of the terms in Eq. (4), we can obtain the preliminary inclusive cross sections σ_0 . However, to make sure that our EG model was realistic and that we did not introduce significant bias in our measurements, we estimated the cross sections iteratively. Our approach was to use the preliminary extracted cross sections σ_0 to modify the EG model, and then to perform new MC simulations to redetermine the acceptance/efficiency, deconvolution, radiative, and bincentering corrections. Using the new R_1 , BC₁, and η_1 obtained with model σ_{sim1} , we computed the cross sections after one iteration σ_1 that made it possible to start the second iteration.

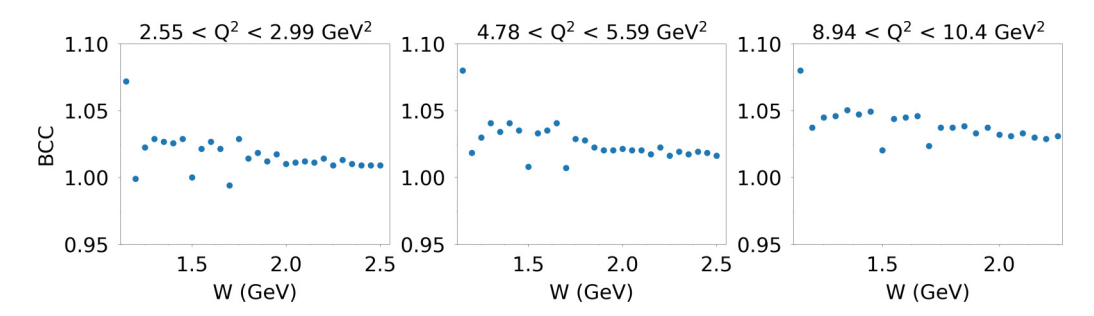


FIG. 17. Bin-centering corrections (BCC) vs W for 3 representative Q^2 bins calculated as the ratio of the mean cross section over the bin to the cross section in the center of the bin.

TABLE II. Listing of the bin limits in Q^2 for each of the nine bins used in this cross-section analysis and the associated values at the geometric center of the bin.

Q^2 Bin limits (GeV ²)	Q^2 Bin center (GeV ²)
2.557–2.990	2.774
2.990-3.497	3.244
3.497-4.089	3.793
4.089-4.782	4.436
4.782-5.592	5.187
5.592-6.539	6.066
6.539-7.646	7.093
7.646-8.942	8.294
8.942-10.456	9.699

Ultimately, we performed three iterations to determine σ_{sim2} and σ_{sim3} , so we ran four sets of simulations and determined the corresponding corrections factors following the standard chain described here.

A. Event generator adjustments

The inclusive EG is based on the Bodek parametrization [7] for the resonance contributions and also includes a built-in function for the background. To come up with a new, more realistic EG, we calculated the χ^2 for all preliminary cross-section data points relative to the EG values (over the full W and Q^2 coverage) and tried to minimize it varying the parameters in the EG model to adjust the initial cross-section model σ_{sim0} . This was done in two steps. In the first step, we varied the background function to come up with the correct normalization. After that, we varied all resonance parameters to align the peak positions, widths, and the evolution of these parameters with Q^2 . The same approach was followed for successive iterations.

B. Iteration comparisons

Several corrections and procedures in the cross-section extraction were introduced or updated after performing the iteration studies through σ_{sim2} . These updates called for an additional iteration that would make our MC simulation up to date. The additional iteration to determine σ_{sim3} was

performed exactly the same way as for the two previous iterations. The EG parametrization was fit to reproduce the extracted cross sections after all of the aforementioned improvements. Using the updated EG, our final acceptance, radiative, and bin-centering corrections were found. This is the most realistic EG possible for this measurement. We would like to point out that since the updates to the cross-section extraction procedure were made, the difference between iteration 2 and 3 comes not only from the iteration procedure itself but also from those updates. The most significant effect of iteration 3 can be seen in the very first W bin, which is the result of an update to the EG elastic cross section.

Four models: initial EG model σ_{sim0} (blue), iteration N=1 σ_{sim1} (green), iteration N=2 σ_{sim2} (orange), and iteration N=3 σ_{sim3} (purple) are shown in Fig. 18. It is seen that the resonance peaks are shifted to slightly lower W values after two iterations. This occurred as the peak position in the initial model and our measurement did not fully coincide. Figure 19 shows the inclusive cross sections σ_3 from the third EG iteration model compared to the σ_{sim3} EG model.

The radiative corrections R_0 obtained with the initial model σ_{sim0} , the R_1 values obtained with the first iteration model σ_{sim1} , and the R_2 values obtained with the second iteration model σ_{sim2} are shown in Fig. 20. A slight shift in the peak position to lower W with increasing iteration number can be seen. This is a result of different peak positions in the measured W distribution and the initial model W distribution. There was no need for more iterations since the different iterations were consistent with each other.

The bin-centering corrections BC_0 obtained with the initial model σ_{sim0} , the BC_1 values obtained with the first iteration model σ_{sim1} , and the BC_2 values obtained with the second iteration model σ_{sim2} are shown in Fig. 21. It is seen that the bin-centering corrections do not change much because there is no significant change in the crosssection shape. There was no need for more iterations since the iterations were consistent with each other.

C. Cross section after iterations

Combining R, BC, and η obtained with the different models, the cross sections for every EG model can be calculated. There is a minimal visible effect on the peaks in the second and third resonance regions comparing the initial cross sections extracted with the original EG model relative to those

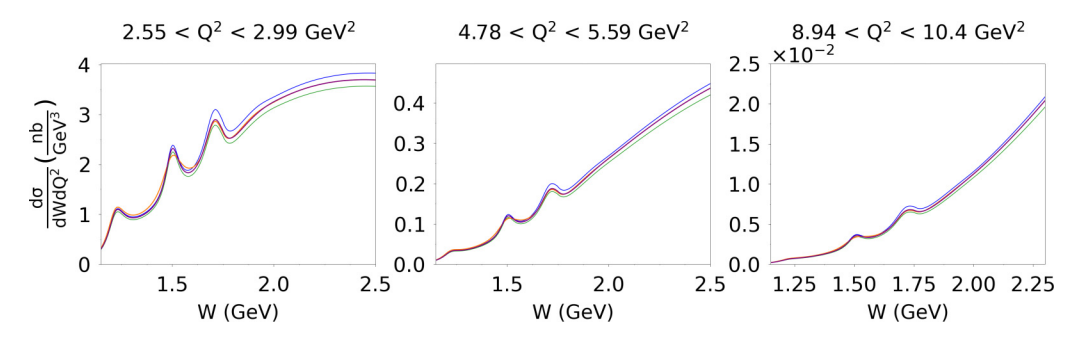


FIG. 18. Initial inelastic model cross section from EG σ_{sim0} (blue), iteration N=1 model σ_{sim1} (green), iteration N=2 model σ_{sim2} (orange), and iteration N=3 model σ_{sim3} (purple) for 3 representative Q^2 bins.

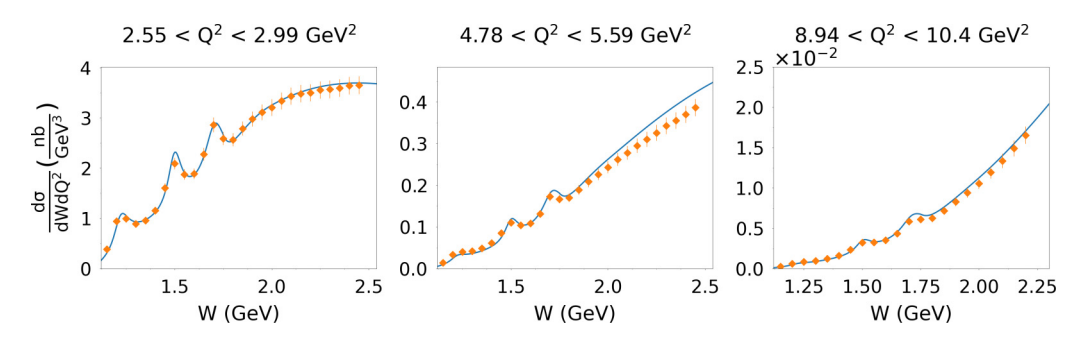


FIG. 19. Inclusive cross sections σ_3 (orange points with error bars) obtained with the iteration 3 model $\sigma_{\text{sim}3}$ (blue curves) for 3 representative O^2 bins.

extracted from the second iteration model. There is no change seen with iteration version where the cross section is smoothly varying. Figure 22 shows the extracted cross sections for each of our iteration models and Fig. 23 shows the ratio of the cross sections after each iteration relative to the original EG model.

VII. STATISTICAL AND SYSTEMATIC UNCERTAINTIES

A. Statistical uncertainties

The CLAS12 forward detector consists of six separate sectors. We extracted cross sections for the scattered electron separately in each sector. As a result we have six separate measurements. For the final cross sections quoted in this work we took the p(e, e')X cross section as the average over all six sectors.

Statistical uncertainties were estimated assuming normal distributions for inclusive electron scattering events with the dispersion $\sqrt{N(W,Q^2)}$ for the number of reconstructed events in the (W,Q^2) bins corrected for detection efficiencies and accounting for acceptance after performing the deconvolution. In the evaluation of the statistical uncertainty of the p(e,e')X cross section we combined the terms in Eq. (4) into sector-dependent $B_i(W,Q^2)$ and sector-independent $A(W,Q^2)$ factors,

$$\frac{d\sigma}{d\Omega} = A(W, Q^2) \sum_{i=1}^{6} \frac{N_i(W, Q^2)}{B_i(W, Q^2)},$$
(17)

where $N_i(W, Q^2)$ is the number of reconstructed events in sector i, $A(W, Q^2)$ is the product of all factors that do not depend

on sector number such as radiative corrections, luminosity, bin-centering corrections, etc., and $B_i(W, Q^2)$ is the product of all factors in sector *i* that depend on sector number (e.g., efficiency corrections).

By employing the error propagation formula, after computing the derivative over N_i in Eq. (17), the statistical uncertainty of $\delta \sigma$ of the cross section can be computed as

$$\delta\sigma(W, Q^2) = A(W, Q^2) \sqrt{\sum_{i=1}^{6} \frac{N_i(W, Q^2)}{B_i(W, Q^2)^2}}.$$
 (18)

If we define $N_{i \text{ corr}}(W, Q^2) = N_i(W, Q^2)/B_i(W, Q^2)$, the relative statistical uncertainties for the averaged cross sections in each bin of (W, Q^2) can be estimated as

$$\frac{\sqrt{\sum_{i=1}^{6} \frac{N_{i \text{ corr}}(W, Q^{2})}{B_{i}(W, Q^{2})}}}{\sum_{i=1}^{6} N_{i \text{ corr}}(W, Q^{2})}.$$
(19)

In this approach, we do not have to consider factors that do not depend on sector number because they will be the same in the numerator and denominator. The statistical uncertainty in each Q^2 bin is on average $\lesssim 0.5\%$ for $Q^2 < 5.59$ GeV². Overall the average statistical uncertainty is below 1%. It increases at high Q^2 and W < 1.3 GeV because of the cross-section shape.

Our reconstructed MC event sample has at least a factor of 5 times more statistics than the data sample for all (W, Q^2) bins, so the statistical uncertainty is dominated by the data events. Given the MC acceptance is computed as $\eta(W, Q^2) = N_{\text{rec}}(W, Q^2)/N_{\text{gen}}(W, Q^2)$, the relative statistical uncertainty of

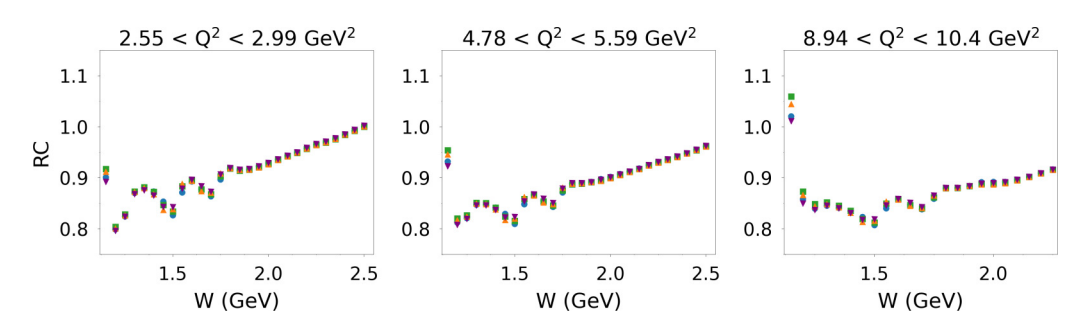


FIG. 20. Radiative corrections R_0 obtained with the initial model $\sigma_{\text{sim}0}$ (blue), the R_1 values obtained with the first iteration model $\sigma_{\text{sim}1}$ (green), the R_2 values obtained with the second iteration model $\sigma_{\text{sim}2}$ (orange), and the R_3 values obtained with the third iteration model $\sigma_{\text{sim}3}$ (purple) for 3 representative bins in Q^2 .

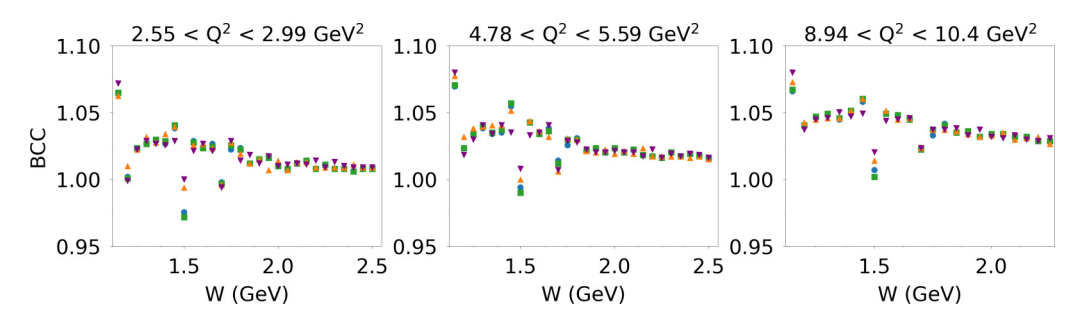


FIG. 21. Bin-centering corrections BC_0 obtained with the initial model σ_{sim0} (blue), the BC_1 values obtained with the first iteration model σ_{sim1} (green), the BC_2 values obtained with the second iteration model σ_{sim2} (orange), and the BC_3 values obtained with the third iteration model σ_{sim3} (purple) for 3 representative Q^2 bins.

the acceptance can be computed as

$$\frac{\delta \eta(W, Q^2)}{\eta(W, Q^2)} = \sqrt{\frac{1}{N_{\text{rec}}(W, Q^2)} + \frac{1}{N_{\text{gen}}(W, Q^2)}}.$$
 (20)

If we propagate this statistical uncertainty to the cross sections $\sigma(W,Q^2) = N_i(W,Q^2)/\eta(W,Q^2)$, assuming that the number of events includes all of the corrections for notation simplification, then we compute the relative statistical uncertainty as

$$\frac{\delta\sigma(W,Q^2)}{\sigma(W,Q^2)} = \sqrt{\left(\frac{\delta N_i(W,Q^2)}{N_i(W,Q^2)}\right)^2 + \left(\frac{\delta\eta(W,Q^2)}{\eta(W,Q^2)}\right)^2}. \quad (21)$$

This statistical uncertainty takes into account both the data and MC. We then used exactly the same approach as in Eqs. (18) and (19). The total statistical uncertainty for all of our analysis bins is shown in Fig. 24.

B. Systematic uncertainties

To estimate the systematic uncertainty for every (W,Q^2) bin, the mean cross sections over all six sectors with different values for each cut or correction were considered, while fixing all other cuts and corrections. In this way we obtained cross-section measurements for loose, nominal, and tight cut versions so we could estimate the effect of a single cut or correction on the final cross sections. For this estimation we used

$$\delta\sigma_{\text{cut}}(W, Q^2) = \frac{|\sigma(W, Q^2) - \sigma_{\text{loose}}(W, Q^2)| + |\sigma(W, Q^2) - \sigma_{\text{tight}}(W, Q^2)|}{2} \frac{1}{\sigma(W, Q^2)},$$
(22)

where $\sigma(W,Q^2)$, $\sigma_{loose}(W,Q^2)$, and $\sigma_{tight}(W,Q^2)$ represent the mean cross sections for the nominal, loose, and tight versions of a cut, respectively. The sources of systematic uncertainty in this analysis are separated into those that vary bin-by-bin and those that affect the overall cross-section scale. In the remainder of this subsection the different contributions are reviewed.

1. Bin-by-bin systematics

Momentum corrections: Momentum corrections were calculated as a multiplicative factor $f_{corr} = \delta P/P + 1$ applied to

the reconstructed momentum. For our estimations, $\delta P/P$ was varied by $\pm 10\%$. The systematic uncertainty was found to be below 1% for every Q^2 bin but the last one, where it is about 1.5%.

<u>z-vertex cuts</u>: Loose and tight vertex-z cuts were applied using $-8.5 < v_z < 2.5$ cm and $-7.5 < v_z < 1.5$ cm, respectively. The systematic uncertainty is below 1% for every W and Q^2 bin.

<u>Fiducial cuts</u>: The DC geometric and ECAL shower containment fiducial cuts were studied using both looser and tighter variations and resulted in a systematic uncertainty be-

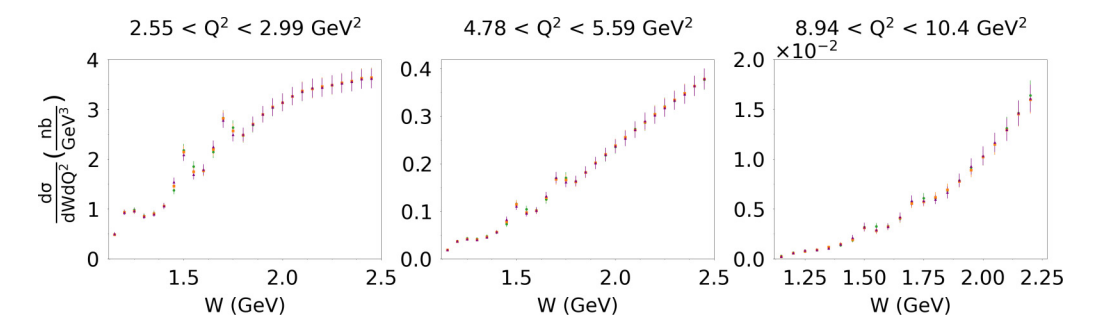


FIG. 22. Cross sections σ_0 obtained with the initial model σ_{sim0} (green), the σ_1 values obtained with the first iteration model σ_{sim1} (orange), and the σ_2 values obtained with the second iteration model σ_{sim2} (purple) for 3 representative bins in Q^2 .

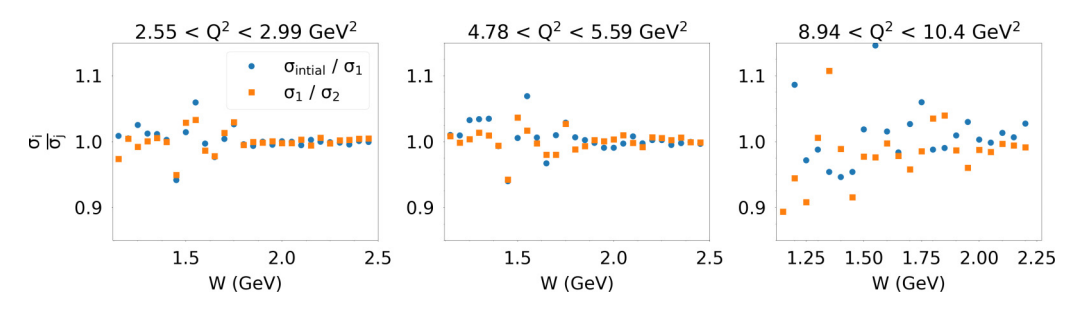


FIG. 23. Ratio of cross sections obtained with the initial model σ_0 to those obtained with the first iteration model σ_{sim1} (blue) and to those obtained with the second iteration model σ_{sim2} (orange) for 3 representative Q^2 bins.

low 1% over all analysis bins. Bad detector element selection was accomplished with ad hoc coordinate cuts based on the different ECAL layers (PCAL, ECin, and ECout) and on angular regions in θ versus ϕ for the DC. The width of these cuts was varied and the systematic difference was found to be below 1% and below 1.5%, respectively, for all analysis bins

Sampling fraction cuts: The energy-dependent ECAL sampling fraction cut nominally at 3.5σ was varied by $\pm 0.5\sigma$. The systematic uncertainty was found to be negligible for all analysis bins. A secondary cut on the PCAL and ECin partial sampling fractions was also included to reduce π^- contamination. This cut was varied and the systematic uncertainty was found to be below 1% for the first 7 Q^2 bins but increased to $\sim 3\%$ at high Q^2 .

<u>Monte Carlo</u>: As the CLAS12 MC gives better resolutions than the data, the reconstructed momentum in the MC was smeared to match the data resolution. To estimate the systematic uncertainty that comes from this procedure, the cross sections were extracted varying the smearing factor by $\pm 5\%$. The systematic uncertainty for smearing was less than 1% on average over all bins.

<u>Deconvolution method</u>: In the analysis two different deconvolution methods, bin-by-bin and Bayesian unfolding, were considered. Our nominal analysis used the Bayesian method because it accounts for multidimensional bin mi-

gration effects. The cross sections were calculated with the bin-by-bin and Bayesian deconvolutions methods while keeping all the other corrections exactly the same. The difference between the two methods resulted in an assigned systematic of 1% on average.

Empty target subtraction: To estimate the systematic uncertainty associated with the contribution of the target end-caps, the empty target contribution with and without the cut removing the v_z region containing just the residual cold gas was estimated. The first approach over-corrects the number of events because it includes the residual cold hydrogen gas in the target cell. It was decided to use 50% of the difference between the two approaches as the systematic uncertainty for this source. Averaging the systematic uncertainty for the empty target contribution subtraction over all kinematic bins gave 0.4%.

Radiative corrections: The radiative corrections were obtained as a result of an iterative procedure. In our analysis, we refit the EG cross-section parametrization using our measurement to give a new EG. The procedure converges and the difference between the last two radiative correction iterations was taken as an estimation of the radiative correction systematic uncertainty. It was found to be <0.5% for all bins.

<u>Bin-centering corrections</u>: The same approach as in the radiative correction case was used for the bin-centering correction systematic uncertainty estimation. The difference

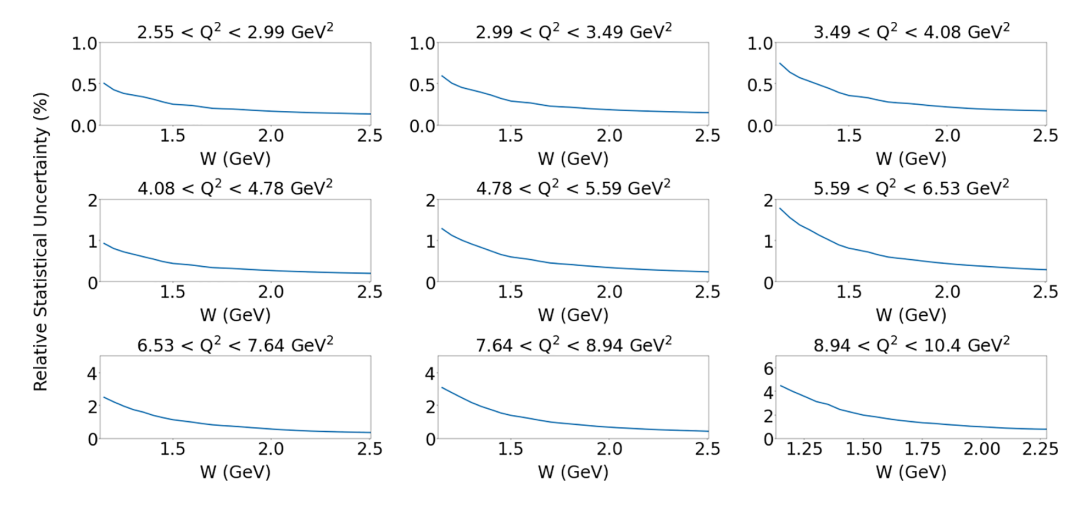


FIG. 24. Relative statistical uncertainty for each of our (W, Q^2) bins calculated using Eq. (19) taking into account the MC statistical uncertainties.

between the last two bin-centering correction iterations was used for the estimation of the systematic uncertainty. The systematic was found to be less than 1% for all bins.

 π^- contamination: To study possible contamination of our electron sample from non-minimum-ionizing π^- that have momenta above threshold to give a signal in the HTCC, $p\gtrsim 5$ GeV, using MC we estimated the ratio of electrons to π^- s that pass our electron identification requirements in our kinematic range of interest. The generator used for these MC studies was CLASDIS [58], which is based on the polarized version of the LEPTO+Jetset (PEPSI) EG [59] that simulates complete events in deep inelastic lepton-nucleon scattering (DIS). Several parameters enter in the tuning of the hadronization process, and those were selected to reproduce the electron, photon, and pion distributions obtained in the CLAS12 RG-A data for the semi-inclusive regime (i.e., $Q^2 > 1$ GeV² and W > 2 GeV).

In our studies we have made several assumptions:

- (1) The DIS process is responsible for the creation of the dominant fraction of high-momentum pions in the RG-A dataset. These pions only appear for $W \gtrsim 2$ GeV.
- (2) The physics model in the CLASDIS EG contains accurate ratios of final state π^- and electrons in its designed deep inelastic scattering kinematic region to quantitatively estimate the π^- contamination for $Q^2 > 1 \text{ GeV}^2$ and W > 2 GeV.
- (3) The contamination of π^- in our electron sample for W > 2 GeV can be used to set an upper limit on the π^- contamination in the entire kinematic range of this analysis for W from 1.125 GeV to 2.5 GeV.

The ratio of π^- s to electrons is in the range from 0.2% to 0.5% with the ratio increasing as the particle momentum decreases.

Charge symmetric background: For e+p scattering, processes that produce charge-symmetric e^+e^- decays can contaminate the inclusive electron sample. The most important source of e^+e^- pairs in CLAS12 is due to the production of π^0 mesons, which either decay to γe^+e^- (Dalitz decay mode) or to $\gamma \gamma$, with the latter branch accounting for 98.8% of the decay fraction. For these processes $\gamma \to e^+e^-$ conversions can occur. These secondary electrons can contaminate the events for the determination of the inclusive electron scattering cross section. We estimated the contribution of this charge symmetric background using two different procedures. One was based directly on the RG-A data and the other was based on available data parametrizations that served as a cross-check.

The contamination of electrons from the charge symmetric background can be estimated directly from the data by examining positrons in the opposite torus polarity dataset collected as part of the same RG-A data run. The positrons in outbending data should behave like the charge symmetric background electrons in inbending data. To study this, the inclusive e^-X signal was investigated in the inbending runs and the inclusive e^+X signal was investigated in the outbending runs.

After applying our complete set of electron identification requirements to both electrons and positrons, the estimation of the charge symmetric background in our inclusive kinematic bins was determined by normalizing the e^+X to e^-X ratio by the ratio of the inbending to outbending dataset Faraday cup charge ratio (see Fig. 25). As a result of this study, the charge symmetric background contamination of our inclusive electron sample was shown to be below 0.5%.

We also estimated the charge symmetric background using the model of Bosted [60] as a cross-check. This model is based on a fit of the inclusive pion photoproduction reaction from SLAC data and has been carefully checked and shown to be in reasonably good agreement with the measured positron cross section. This model was used in the inclusive analysis of CLAS data by Osipenko [8] and in the inclusive analysis of Hall C data by Malace [9].

The code generates π^0 s over the full kinematic range of the CLAS12 RG-A data and then decays $\pi^0 \rightarrow \gamma \gamma$ over all possible polar angles and energies. Finally, it accounts for e^+e^- photoproduction. To estimate the contribution of the charge symmetric background electrons relative to the inclusive electrons as a function of kinematics, an estimate of the ratio of the cross section for the charge symmetric electrons to the Born cross section is required. To do this the code selects the charge symmetric background electrons in our (W, Q^2) bins at the input beam energy. The computation shows that we do not have any significant contamination (less than 0.1%) because W is less than 2.525 GeV for all but the last Q^2 bin, where it is limited to 2.275 GeV. The minimum momentum of electrons in our analysis is more than 2.77 GeV, while the charge symmetric background electrons have lower momenta in general. This finding is consistent with the code output and is also consistent with the results based on the RG-A data.

Torus field map: Different finite-element analysis models of the CLAS12 torus magnetic field were available for study based on an ideal model of the torus coil geometry and on a model based on survey measurements of the actual coils during their manufacture. Details on the field map for the torus are included in Ref. [61]. For most of our analysis bins the difference in the cross sections between these two models was below 3%, so this difference was assigned as a systematic uncertainty.

Sector-dependent studies: In inclusive electron scattering, there is no ϕ dependence in the production amplitude, which should result in uniform cross sections over the azimuthal angle ϕ . The CLAS12 forward detector consists of six sectors that divide the azimuthal acceptance such that each sector has azimuthal coverage varying from 50% of $2\pi/6$ at 5° to 80% of $2\pi/6$ at 40° . However, not all of the sectors shared the same configuration in this dataset. Sectors 1, 2, and 6 had no additional forward carriage detectors in front of FTOF, while sectors 3, 4, and 5 had Cherenkov detectors installed. The different detector configurations, nonideal knowledge of the magnetic field, imperfect understanding of the detector alignment, various inefficiencies, and the presence of hot or weak detector channels, can lead to sector-to-sector variations. Some cuts and corrections are sector dependent to account for known inefficiencies or sector properties. Ultimately, there are six independent measurements of the inclusive cross sections. The differences between them are reported as a systematic

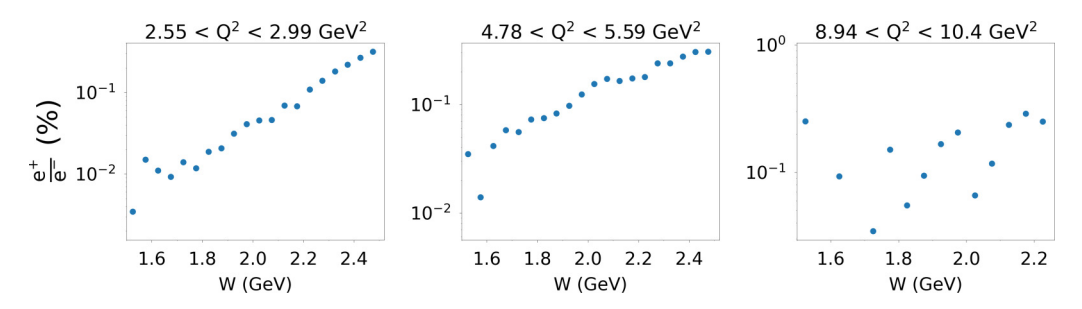


FIG. 25. Ratio of positron events from the RG-A outbending dataset to the electron events from the RG-A inbending dataset (in percent) vs W for 3 representative Q^2 bins after applying all cuts from this analysis.

uncertainty. The sector dependence is estimated as the corrected sample standard deviation over all six sectors, i.e.,

$$\delta\sigma_{\text{sec}}(W, Q^2) = \sqrt{\frac{1}{5} \sum_{i=1}^{6} (\sigma_{\text{mean}}(W, Q^2) - \sigma_{\text{sec}_i}(W, Q^2))^2 \frac{1}{\sigma_{\text{mean}}(W, Q^2)}},$$
(23)

where $\sigma_{\rm mean}(W,Q^2)$ is the average cross section over the six sectors and $\sigma_{{\rm sec}_i}(W,Q^2)$ is the cross section determined for sector i. The sector dependence is $\approx 5\%$ for $Q^2 < 6.53$ GeV². It starts to increase with Q^2 and reaches up to 15% for W < 1.4 GeV in the last Q^2 bin, but for W > 1.7 GeV, it is below 5% for all Q^2 bins. This sector dependence is the dominant source of bin-by-bin systematic uncertainty in our measurement.

2. Scale-type systematics

Beam charge: The integrated beam charge has two sources of systematic uncertainty. The first is a 1% uncertainty associated with the calibration of the charge integrator on the Faraday cup. The second is a 0.6% uncertainty associated with the finite number of charge readings within the data file and with how these charge readings are unpacked in the reconstruction code. Combining these two sources gives an assigned scale systematic uncertainty of 1.2% on the measured Faraday cup charge.

Background merging: The simulations for this analysis employed a background merging approach to best match the backgrounds in the various CLAS12 detector subsystems. The studies of this procedure comparing track reconstruction efficiency in data and MC as a function of beam current resulted in a 3% scale uncertainty in the tracking efficiency in the CLAS12 forward detector.

Target thickness: Finite element analysis of the RG-A cryotarget both in its room temperature configuration and at its operating temperature were performed. The 5.0-cm-long target has 30- μ m-thick aluminum entrance and exit windows. The cell base, base tube, and Kapton are epoxied to a fixture, and their location is within 0.5 mm of the model dimensions in z. The cell is manufactured by prebowing the end windows to minimize stresses at its operating temperature and pressure. The mechanical tolerance is quoted as 5.00 ± 0.05 cm for a systematic uncertainty of 1% on the overall target length. The consideration of the thermal expansion of the different materials in the target assembly was shown to have a much

smaller effect on the target cell length uncertainty compared to the mechanical tolerance and was neglected. Also included in this contribution is the uncertainty on the average liquid-hydrogen target thickness from the fluctuations of the pressure and temperature variations during the experiment. This gives rise to a scale uncertainty of 1.5%.

3. Total systematic uncertainty

The total systematic uncertainty is the quadrature sum of the aforementioned sources,

$$\delta\sigma_{\text{total}}(W, Q^2) = \sqrt{\sum_{i=1}^{N_{\text{sources}}} \delta\sigma_i(W, Q^2)^2}, \tag{24}$$

where the sum runs over the N_{sources} of systematic uncertainty and $\delta \sigma_i(W, Q^2)$ is the systematic uncertainty associated with source i in %.

The relative total systematic uncertainty as a function of W for all Q^2 bins is shown in Fig. 26. The systematic uncertainties averaged over all Q^2 and W are given in Table III. The average bin-by-bin systematic uncertainty for this inclusive cross-section measurement is 5.8% and the total scale uncertainty is 3.7%.

VIII. RESULTS AND DISCUSSION

In this section we present our final inclusive electron scattering cross sections. Our starting point is a comparison of the CLAS12 results with the previous CLAS results measured for W < 2.0 GeV and $Q^2 < 3.6$ GeV² [8] shown in Fig. 27. Figure 28 compares the (Q^2, W) kinematic coverage of the CLAS data (shown by the green lines) to our CLAS12 data (shown by the orange points). The CLAS results were interpolated into the (W, Q^2) grid of our experiment accounting for the difference in electron beam energy. This difference has an impact on both the virtual photon flux Γ_v and the virtual photon polarization parameter ϵ defined by Eqs. (10) and (11) in Ref. [62]. The unpolarized cross sections σ_U were computed from the CLAS results on the F_2 structure function according

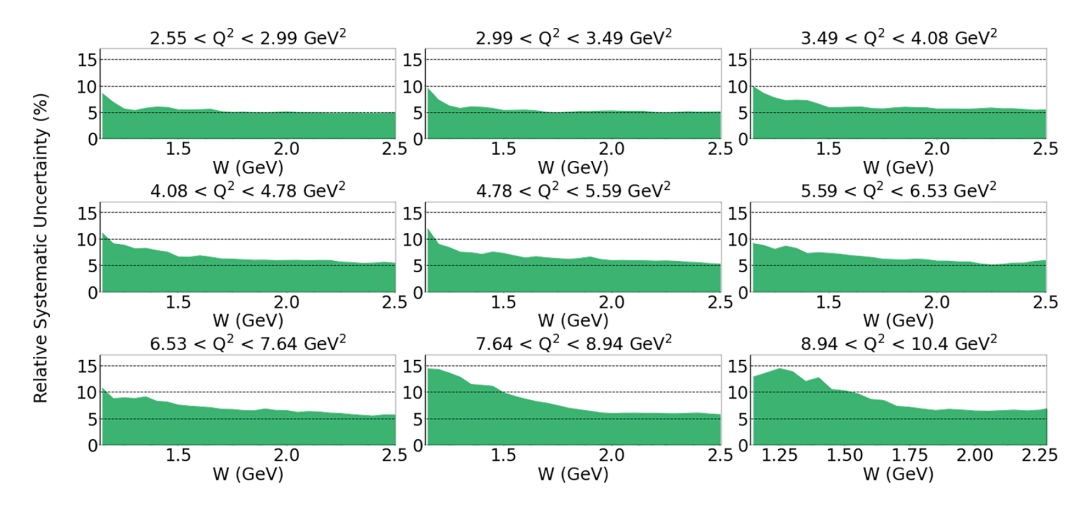
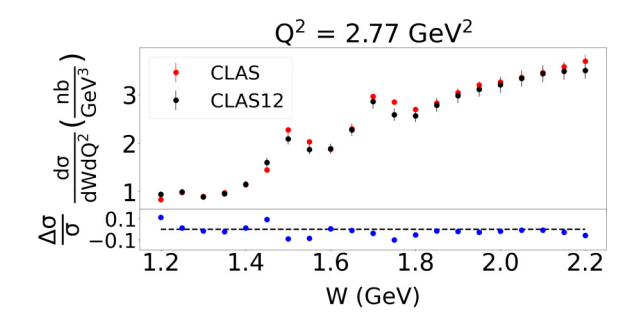
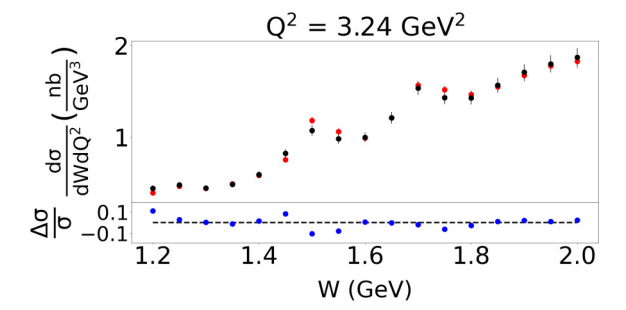


FIG. 26. Total relative systematic uncertainty for all of our (W, Q^2) bins. The black dashed lines show the 5%, 10%, and 15% levels.





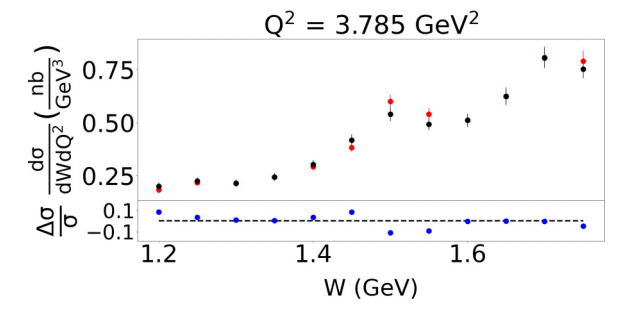


FIG. 27. Comparison of the CLAS12 inclusive electron scattering cross sections from this work (black points) to those from CLAS (red points) [8] after interpolation into the kinematic grid of our experiment. The bottom subplot with each Q^2 bin shows the relative cross-section difference, $(\sigma_{\text{CLAS}12} - \sigma_{\text{CLAS}})/\sigma_{\text{CLAS}12}$, between the two measurements with the dashed line at zero. The error bars shown on all of the data are the quadrature sum of the statistical and systematic uncertainties.

to Eq. (25) with parameter ϵ for the CLAS12 measurements and the ratio $R_{LT} = \sigma_L/\sigma_T$ taken from Ref. [63]:

$$F_2(W, Q^2) = \frac{KM}{4\pi^2 \alpha} \frac{2x}{\rho^2} \frac{1 + R_{LT}}{1 + \epsilon R_{LT}} \, \sigma_U(W, Q^2), \tag{25}$$

where

$$\sigma_U(W, Q^2) = \sigma_T(W, Q^2) + \epsilon \, \sigma_L(W, Q^2). \tag{26}$$

TABLE III. Systematic uncertainty for the inclusive p(e, e')X cross sections averaged over all (W, Q^2) kinematic bins.

Average systematic uncertainty		
Bin-by-bin sources	Uncertainty [%]	
Sampling fraction cut	0.02	
Pion contamination	0.1	
PCAL fiducial cut	0.12	
Momentum smearing	0.28	
Bin-centering corrections	0.32	
Empty target subtraction	0.33	
Radiative corrections	0.36	
Momentum corrections	0.46	
Charge symmetric background	0.5	
Deconvolution method	0.55	
Vertex-z cut	0.57	
DC fiducial cut	0.72	
Electron pion separation cut	0.79	
Torus field map	3.0	
Sector dependence	4.41	
Total bin-by-bin	5.8	
Scale type sources	Uncertainty [%	
Beam charge uncertainty	1.2	
Target thickness uncertainty	1.8	
Background merging	3.0	
Total scale	3.7	

6.9

Total bin-by-bin and scale

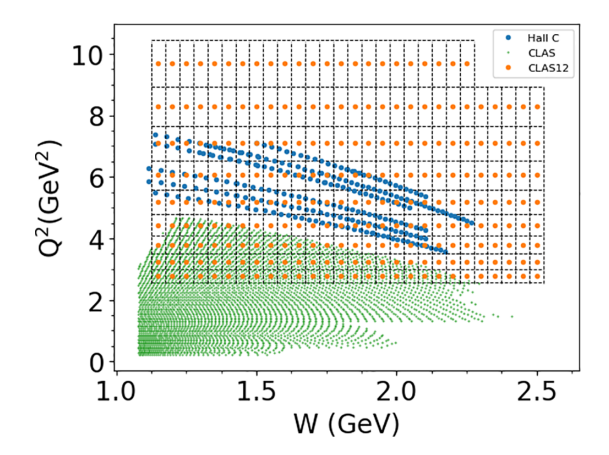


FIG. 28. Comparison of the kinematic coverage of the CLAS (shown by the green lines) and Hall C p(e, e')X cross sections (shown by the blue points) from Refs. [8] and [9], respectively, to that from this analysis of CLAS12 RG-A data (shown with the bin centered values at the orange points within the defined bins shown by the grid) in terms of Q^2 vs W.

Here $\alpha = 1/137$ and ρ is a kinematic parameter given by

$$\rho^2 = 1 + \frac{4M^2x^2}{O^2}. (27)$$

K is the equivalent photon energy, defined here in the Hand convention as

$$K = \frac{W^2 - M^2}{2M},\tag{28}$$

and

$$x = \frac{Q^2}{2M\nu},\tag{29}$$

where M is the proton mass and ν is the virtual photon energy in the laboratory frame.

The unpolarized cross sections σ_U deduced from the CLAS measurement of the F_2 structure function correspond to the electron beam energy of the CLAS12 measurements of 10.6 GeV. The CLAS data shown in Fig. 27 were computed as the product of the virtual photon flux and the unpolarized σ_U cross section for a beam energy of 10.6 GeV.

All details of the interpolation/extrapolation of the inclusive structure functions can be found in Ref. [64]. The website of Ref. [65] provides for an evaluation of the interpolated p(e,e')X observables onto a (W,Q^2) kinematic grid for an incoming electron beam energy defined by the user for W < 2.0 GeV and $Q^2 < 7.0$ GeV². Our new CLAS12 measurement is consistent within uncertainties with the previous CLAS measurement.

Measurements of the inclusive p(e, e')X cross sections in the resonance region were also carried out in Hall C at JLab with a small-acceptance spectrometer at high luminosity achieved with an electron beam current up to $100 \mu A$ [9]. Because of the small acceptance of the Hall C spectrometer, those inclusive cross sections are only available within bins for highly correlated values of W and Q^2 shown by the blue data points in Fig. 28 compared to the kinematic coverage of

our CLAS12 data. The Hall C data below W = 2.5 GeV are only available within the limited Q^2 range from 3.5–7.5 GeV² in comparison with the CLAS12 RG-A results obtained for Q^2 from 2.55-10.4 GeV². Furthermore, the large electron scattering angle acceptance of CLAS12 allowed us to obtain the p(e, e')X cross sections for each given Q^2 bin with a broad coverage over W from the pion threshold up to 2.5 GeV. This feature is important for the exploration of the Q^2 evolution of the partonic structure of the nucleon ground states. However, the high luminosity and better resolutions achievable in the Hall C measurements allows for exploration of both the W and Q^2 evolution of the p(e, e')X cross sections in more detail, collecting data for finer (W, Q^2) bins than achievable in our CLAS12 measurements. Therefore, a combined analysis of the p(e, e')X cross sections from CLAS12 and Hall C would be beneficial for gaining insight into the structure of the nucleon ground states at large values of the fractional parton momenta x in the resonance region. In addition, the p(e, e')Xdata obtained at different beam energies in the measurements with CLAS12 and in Hall C for a given (W, Q^2) bin offer the opportunity for separation between the longitudinal and transverse contributions to the unpolarized virtual photon + proton cross sections.

A comparison between the CLAS12 RG-A and Hall C p(e, e')X cross sections was carried out. The σ_U cross sections were derived from the Hall C $d\sigma/d\Omega dE'$ crosssection data [9] by multiplying the inverse virtual photon flux values $1/\Gamma_v$ for the kinematics in the Hall C measurements. The σ_T and σ_L contributions were deduced from σ_U in a similar way as described above for the CLAS results. After that, the σ_U cross sections were reevaluated from the σ_T and σ_L components with ϵ computed using the beam energy E_b and (W, Q^2) from the CLAS12 data. Finally, the appropriate Jacobian was introduced. Appropriately selected data points from the Hall C measurement were compared to the CLAS12 cross sections for those bins satisfying the criteria $\Delta Q^2 < 0.1$ GeV² and $\Delta W < 0.01$ GeV. In total there are 16 data points for which a comparison between the two datasets can be made. Figure 29 shows a direct comparison of the cross sections from the two measurements for these selected kinematic points. The two datasets are in agreement within uncertainties for most data points. However, there is a some tension in the comparison for the $Q^2 = 6.1 \,\text{GeV}^2$ bin where the scale difference is ~25%, although it should be pointed out that number of points for comparison is much fewer in the bins at $Q^2 = 6.1 \,\text{GeV}^2$ and $7.2 \,\text{GeV}^2$ compared to $Q^2 = 5.2 \,\text{GeV}^2$. The data points from Hall C within the (W, Q^2) bins of the RG-A CLAS12 measurements offer complementary information on the cross-section evolution within these bins that can be used in the future for improvement in the evaluation of the averaged cross sections.

Our final results for the extracted cross sections from the CLAS12 RG-A dataset are shown in Fig. 30. These data are also included into the CLAS Physics Database [66]. The cross sections $d\sigma/dWdQ^2$ are shown as a function of W over the range from 1.125 to 2.525 GeV in 50-MeV-wide bins for our nine bins of Q^2 from 2.55 to 10.4 GeV². Our analysis includes a bin centering correction to evolve the measured cross sections to the geometric centers of the given W and Q^2 bins.

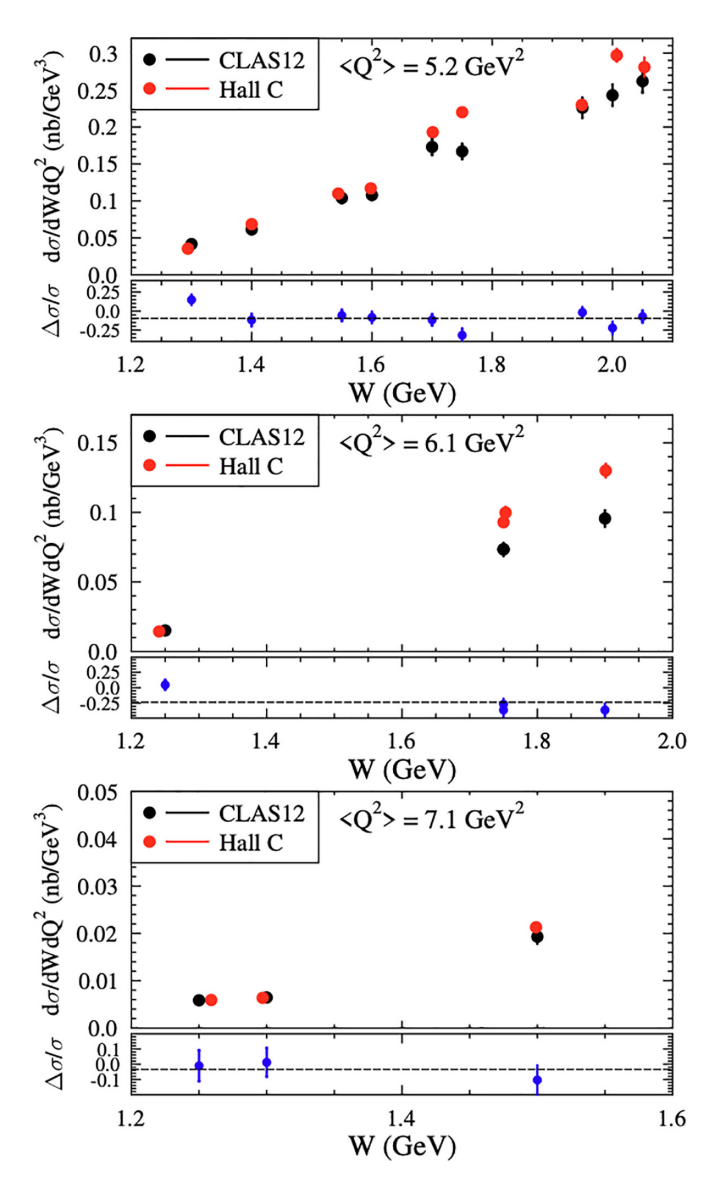


FIG. 29. Comparison of the CLAS12 inclusive electron scattering cross sections from this work to those from Hall C [9]. The Hall C data have been converted from $d\sigma/d\Omega dE'$ to $d\sigma/dW dQ^2$ as described in the text accounting for the different Hall C beam energy (5.5 GeV) compared to this CLAS12 dataset (10.604 GeV). Only selected data points from the Hall C measurement were compared to the CLAS12 cross sections satisfying $\Delta Q^2 < 0.1 \ \text{GeV}^2$ and $\Delta W < 0.01 \ \text{GeV}$. The data can be compared for 3 average Q^2 bins of 5.2 GeV² (top), 6.1 GeV² (middle), and 7.1 GeV² (bottom). The bottom subplot with each Q^2 bin shows the relative cross-section difference, $(\sigma_{\text{CLAS12}} - \sigma_{\text{Hall C}})/\sigma_{\text{CLAS12}}$, between the two measurements with the dashed line representing the average difference for each Q^2 bin. The error bars shown on all of the data are the quadrature sum of the statistical and systematic uncertainties.

The statistical uncertainties on the CLAS12 data are shown but they are smaller than the data point size for the majority of the data points. The bin-by-bin systematic uncertainty is shown by the filled area at the bottom of each plot.

The CLAS12 measurements of the inclusive electron scattering cross sections as a function of W for selected bins

in Q^2 are shown in Fig. 31. The values of Q^2 selected for display range from 2.77 to 4.43 GeV². The error bars shown are statistical only. The blue points represent the resonance contributions evaluated from the CLAS results on the resonance electrocouplings available from the studies of πN , ηN , and $\pi^+\pi^-p$ electroproduction off protons within the framework of the approach developed in Refs. [26,27]. The resonant amplitudes were computed within the Breit-Wigner ansatz with the $\gamma_v p N^*$ electrocouplings available from the studies of meson electroproduction data in the resonance region [20]. The N^* total decay widths were taken from the experiments with hadronic probes reported in the PDG [67]. So far this is the only available evaluation of the resonant contributions from the experimental results on the N^* electrocouplings and their hadronic decay widths. Currently, as the resonance electrocouplings from the available CLAS data span the mass range of W < 1.75 GeV, the blue points do not extend beyond this value. The resonant contributions to the inclusive p(e, e')X cross sections remain significant over the entire range of $Q^2 < 5 \text{ GeV}^2$ where the experimental results on the N^* electrocouplings are available.

The unique capability of the CLAS12 detector in providing the inclusive electron scattering observables in the full range of W from the pion threshold to 2.5 GeV at any given Q^2 opens up promising opportunities for the exploration of the ground state nucleon PDFs at large x in the resonance region with the resonant contributions estimated from experimental data. The structures seen in the p(e, e')X data in Fig. 31 in the first, second, and third resonance regions for $Q^2 < 5 \text{ GeV}^2$ are related to the resonant contributions. The three resonance region peaks demonstrate pronounced differences in their evolution with Q^2 because of differences in the Q^2 evolution of the electrocouplings of the contributing N^* and Δ^* states. This observation emphasizes the importance of obtaining information on the electrocouplings of all prominent resonances to enable a credible evaluation of the resonant contributions into the p(e, e')X cross sections. Notably, the resonance-like structures in Fig. 30 are clearly seen over the entire range of Q^2 covered in the CLAS12 data, suggesting opportunities for extraction of the N^* electrocouplings for Q^2 up to 10 GeV² from the studies of the exclusive electroproduction channels.

The relative contributions from the three resonance-like peaks seen in the (e, e'X) cross sections in Fig. 30 demonstrate a different evolution with Q^2 . The relative resonant contributions in the first and second resonance maxima remain almost Q^2 -independent, while the relative resonant contribution in the third maximum decreases with Q^2 . The CLAS results on the $\gamma_{\nu}pN^*$ electrocouplings deduced from the exclusive meson electroproduction data [20,21] for the first time allow us to shed light on the contributions from the individual resonances into the resonance-like structures and to understand the features in the Q^2 -evolution of their contributions seen in these inclusive cross sections.

Figure 32 shows the decomposition of the different resonance contributions to the resonant cross section for the same selected Q^2 bins [26,27]. Each of the three resonance region maxima seen in our data arise from several excited states of the nucleon. Even the first resonance maximum, which is dominated by the $\Delta(1232)3/2^+$, has significant $N(1440)1/2^+$

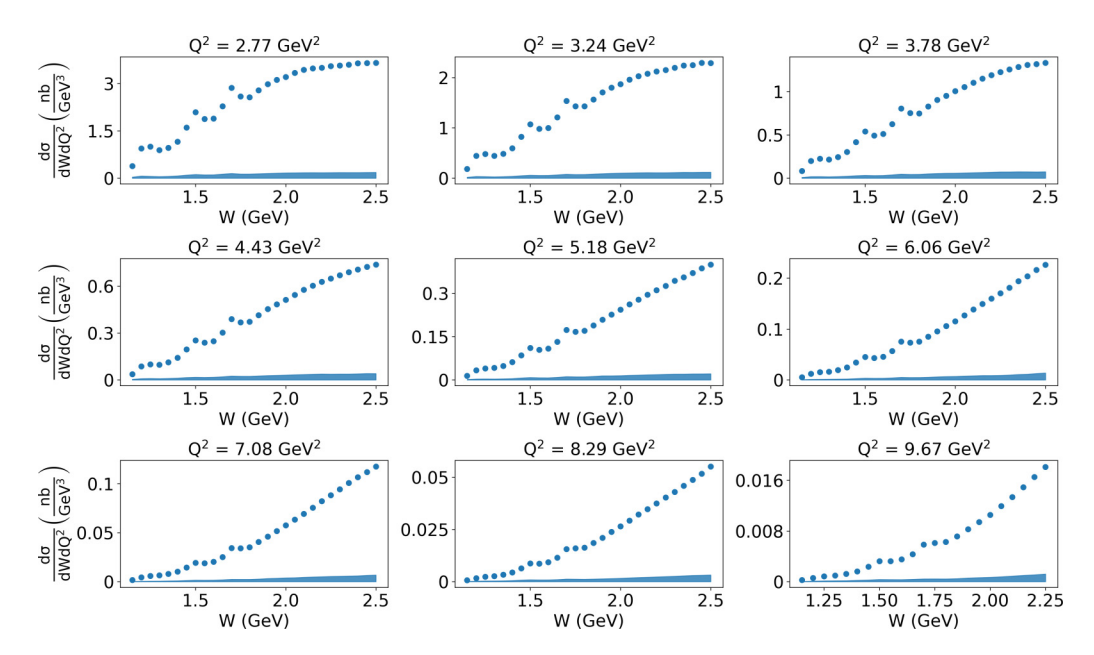


FIG. 30. Inclusive electron scattering cross sections determined from CLAS12 RG-A data. The statistical uncertainties on the CLAS12 data are shown but they are smaller than the data point size for the majority of the data points. The bin-by-bin systematic uncertainty is shown by the filled area at the bottom of each plot.

contributions. The second resonance region maximum is created by the $N(1440)1/2^+$, $N(1520)3/2^-$, and $N(1535)1/2^-$. The third resonance region maximum comprises several nucleon excited states as shown in Fig. 32, with the biggest contribution from the new $N'(1720)3/2^+$ baryon state that was discovered from the combined studies of $\pi^+\pi^-p$ photoand electroproduction data measured in the experiments of 6-GeV era with CLAS [68]. The resonant cross sections show a pronounced evolution with Q^2 in the first, second, and third resonance regions, although they show a stronger Q^2 fall-off in the third resonance regions compared to the second. This suggests that the different excited nucleon states display distinctively different structural features in the Q^2 evolution of

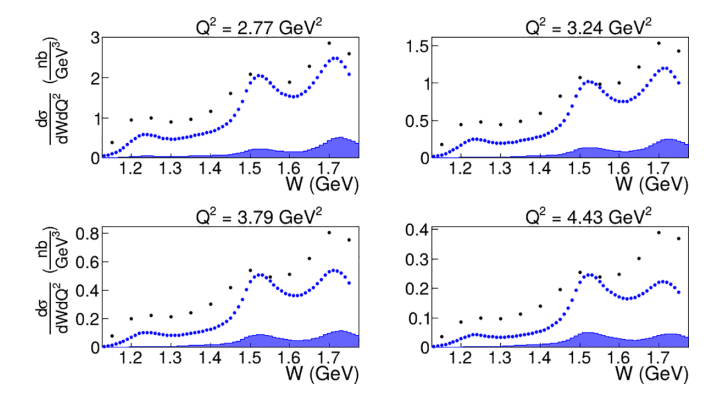


FIG. 31. Inclusive electron scattering cross sections from CLAS12 data at a beam energy of 10.6 GeV as a function of W for selected bins in Q^2 as shown. The blue points represent the computed resonant contributions from the experimental results on the resonance electrocouplings from the studies of πN , ηN , and $\pi^+\pi^-p$ electroproduction off protons with CLAS [26,27]. The shaded areas at the bottom of each plot show the systematic uncertainties for the evaluation of the resonant contributions.

their electrocouplings. This underscores the necessary efforts on the extraction of the N^* electrocouplings of all prominent resonances for $Q^2 > 4$ GeV² from the upcoming data from CLAS12, bridging the efforts between analyses in the N^* and deep inelastic physics regimes [69,70].

Combined studies of the experimental results on the inclusive cross sections and the evaluated resonant contributions open new opportunities for gaining insight into the portion of the inclusive cross sections that is defined by the PDFs in the ground state of the nucleon. Methods to access this component of the inclusive cross sections are currently under development. The measured (e, e'X) cross sections, together with the evaluated resonant contributions, provide the critical experimental input needed to extend our knowledge of PDFs at larger x values within the resonance excitation region.

Our data on the inclusive p(e, e')X cross section allow for extraction of the inclusive F_2 structure function in any given bin of Q^2 within the coverage over W from the pion threshold up to 2.5 GeV. Consequently, the truncated moments of the F_2 structure function can be obtained by direct integration of the data at each given Q^2 . The information on the evolution of the truncated F_2 structure function moments within the resonance region over the broad range of Q^2 covered in our measurements will allow us for the first time to explore the evolution of the partonic structure of the ground state of the nucleon for large values of x within the resonance excitation region in the range of distances where the transition from strongly coupled to perturbative QCD regimes is expected [25,69,71].

IX. SUMMARY AND CONCLUSIONS

In this paper we present results from the first absolute cross-section measurements with the new large-acceptance CLAS12 spectrometer in Hall B at Jefferson Lab. Inclusive

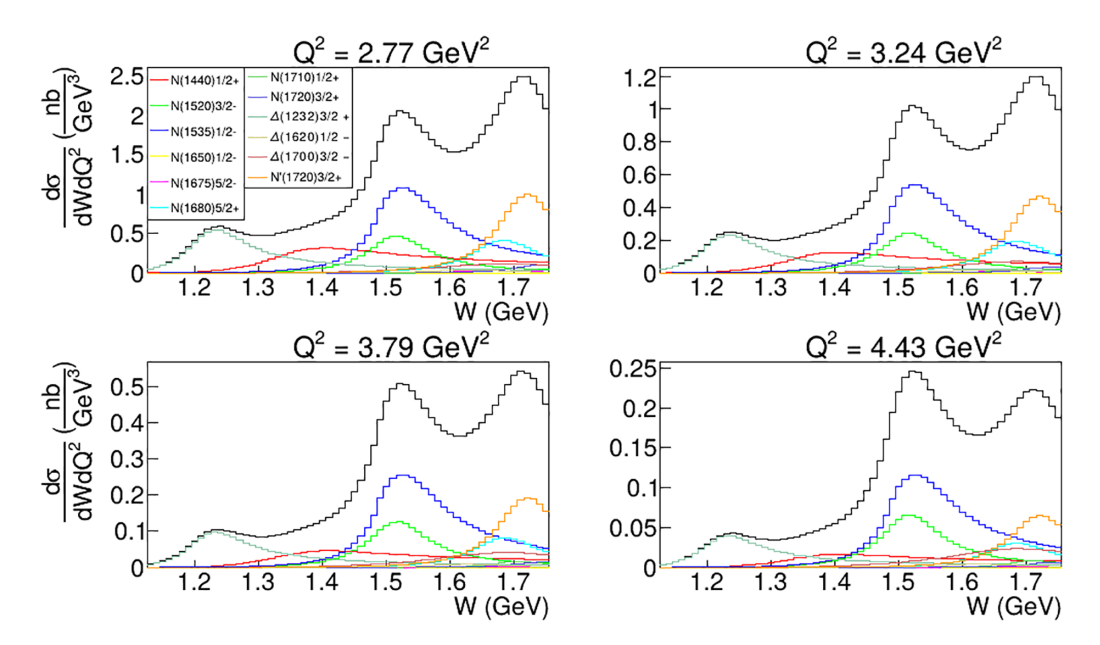


FIG. 32. Decomposition of the total resonant contribution (black curves) to the inclusive electron scattering cross section in the resonance region at different Q^2 for a beam energy of 10.6 GeV, showing the separate contributions of each resonance in the mass range up to 1.75 GeV (see legend on the plots).

electron scattering cross sections are provided over a broad range of invariant mass of the final state hadrons W from 1.125 to 2.525 GeV and four-momentum transfer squared (or photon virtuality) Q^2 from 2.55 to 10.4 GeV² collected at a beam energy of 10.6 GeV. The measured cross sections agree well with the world data available at W from the πN threshold to 2.5 GeV for O^2 from 2.5–7.0 GeV² [8,9]. The large electron scattering angle acceptance of the CLAS12 detector makes it possible in each bin of Q^2 to cover the entire range of W from the πN threshold to 2.5 GeV. The wide W-coverage at any given Q^2 is of particular importance for extending insight into the ground state nucleon partonic structure at large values of fractional parton momenta x within the resonance excitation region. The broad coverage over Q^2 allows for exploration of the evolution of the partonic structure of the nucleon within the range of distances where the transition from the strongly coupled to perturbative QCD regimes is expected [35,70].

The CLAS results on the electroexcitation amplitudes of most excited nucleon states in the mass range up to 1.8 GeV for $Q^2 < 5$ GeV² allow for the evaluation of the resonance contribution into the inclusive electron scattering observables [26–28]. The realistic evaluation of the resonance contributions into the inclusive p(e,e')X cross sections with the N^* electrocouplings and hadronic decay widths available from the experimental data extends the capabilities for understanding the ground state nucleon partonic structure within the resonance region and its evolution with distance. The structures in the first, second, and third resonance regions observed in the W-dependence of the inclusive p(e,e')X cross sections measured with CLAS12 over the range of $Q^2 <$

10 GeV² suggest the opportunity to extend the information on the Q^2 evolution of the nucleon resonance electrocouplings for Q^2 over this full range from the measurements of exclusive meson electroproduction in the resonance region that are currently in progress for data collected with CLAS12. Furthermore, these results offer a new opportunity to extend the scope for the exploration of quark-hadron duality [14].

ACKNOWLEDGMENTS

The authors acknowledge the outstanding efforts of the JLab staff that made this experiment possible. This work was supported in part by the Chilean Comisión Nacional de Investigación Científica y Tecnológica (CONICYT), the Italian Istituto Nazionale di Fisica Nucleare, the French Centre National de la Recherche Scientifique, the French Commissariat à l'Energie Atomique, the Scottish Universities Physics Alliance (SUPA), the United Kingdom's Science and Technology Facilities Council, the National Research Foundation of Korea, and the Skobeltsyn Nuclear Physics Institute and Physics Department at the Lomonosov Moscow State University. This work was supported in part by the U.S. Department of Energy, Office of Science, Office of Nuclear Physics under Contract No. DE-AC05-06OR23177 and the National Science Foundation (NSF) under Grants No. PHY 10011349 and No. PHY 2209421.

DATA AVAILABILITY

The data that support the findings of this article are openly available [66].

^[1] A. Accardi, L. T. Brady, W. Melnitchouk, J. F. Owens, and N. Sato, Phys. Rev. D 93, 114017 (2016).

^[2] S. I. Alekhin et al., Phys. Rev. D 96, 014011 (2017).

^[3] R. D. Ball *et al.* (NNPDF Collaboration), Eur. Phys. J. C 77, 663 (2017).

^[4] J. Gao, L. Harland-Lang, and J. Rojo, Phys. Rep. 742, 1 (2018).

- [5] H. Georgi and H. D. Politzer, Phys. Rev. D 14, 1829 (1976).
- [6] I. Schienbein et al., J. Phys. G 35, 053101 (2008).
- [7] A. Bodek et al., Phys. Rev. D 20, 1471 (1979).
- [8] M. Osipenko et al. (CLAS Collaboration), Phys. Rev. D 67, 092001 (2003).
- [9] S. P. Malace et al., Phys. Rev. C 80, 035207 (2009).
- [10] V. Tvaskis et al., Phys. Rev. C 97, 045204 (2018).
- [11] Y. Liang *et al.* (Jefferson Lab E94-110 Collaboration), Phys. Rev. C 105, 065205 (2022).
- [12] B. A. Mecking *et al.*, Nucl. Instrum. Methods Phys. Res., Sect. A **503**, 513 (2003).
- [13] M. E. Christy and P. E. Bosted, Phys. Rev. C 81, 055213 (2010).
- [14] W. Melnitchouk, R. Ent, and C. Keppel, Phys. Rep. 406, 127 (2005).
- [15] E. D. Bloom and F. J. Gilman, Phys. Rev. Lett. 25, 1140 (1970).
- [16] E. D. Bloom and F. J. Gilman, Phys. Rev. D 4, 2901 (1971).
- [17] I. G. Aznauryan and V. D. Burkert, Prog. Part. Nucl. Phys. 67, 1 (2012).
- [18] V. I. Mokeev *et al.* (CLAS Collaboration), Few-Body Syst. 59, 46 (2018).
- [19] V. I. Mokeev *et al.* (CLAS Collaboration), EPJ Web Conf. 241, 03003 (2020).
- [20] D. S. Carman, K. Joo, and V. I. Mokeev, Few-Body Syst. 61, 29 (2020).
- [21] V. I. Mokeev et al., Phys. Rev. C 108, 025204 (2023).
- [22] V. I. Mokeev and D. S. Carman, Nuovo Cimento C 47, 216 (2024).
- [23] V. I. Mokeev *et al.* (CLAS Collaboration), Phys. Rev. C 86, 035203 (2012).
- [24] V. I. Mokeev et al., Phys. Rev. C 93, 025206 (2016).
- [25] D. S. Carman, R. W. Gothe, V. I. Mokeev, and C. D. Roberts, Particles 6, 416 (2023).
- [26] A. N. Hiller Blin et al., Phys. Rev. C 100, 035201 (2019).
- [27] A. N. Hiller Blin, W. Melnitchouk, V. I. Mokeev, V. D. Burkert, V. V. Chesnokov, A. Pilloni, and A. P. Szczepaniak, Phys. Rev. C 104, 025201 (2021).
- [28] A. N. Hiller Blin, V. I. Mokeev, and W. Melnitchouk, Phys. Rev. C 107, 035202 (2023).
- [29] V. D. Burkert et al. (CLAS Collaboration), Nucl. Instrum. Methods Phys. Res., Sect. A 959, 163419 (2020).
- [30] Y.-Q. Ma and J. W. Qiu, Phys. Rev. Lett. **120**, 022003 (2018).
- [31] A. V. Radyushkin, Int. J. Mod. Phys. A 35, 2030002 (2020).
- [32] K. Orginos, A. Radyushkin, J. Karpie, and S. Zafeiropoulos, Phys. Rev. D 96, 094503 (2017).
- [33] H-W. Lin, PoS LHCP2021, 352 (2021).
- [34] C. Alexandrou, J. Phys.: Conf. Ser. 2586, 012001 (2023).
- [35] Y. Lu et al., Phys. Lett. B 830, 137130 (2022).
- [36] P.-L. Yin et al., Chin. Phys. Lett. 40, 091201 (2023).
- [37] J. Segovia et al., Few-Body Syst. 59, 26 (2018).
- [38] C. Mezrag et al., Phys. Lett. B 783, 263 (2018).
- [39] V. D. Burkert, Annu. Rev. Nucl. Part. Sci. 68, 405 (2018).
- [40] V. D. Burkert, EPJ Web Conf. 241, 01004 (2020).
- [41] M. D. Mestayer et al., Nucl. Instrum. Methods Phys. Res., Sect. A 959, 163518 (2020).

- [42] Y. G. Sharabian *et al.*, Nucl. Instrum. Methods Phys. Res., Sect. A 968, 163824 (2020).
- [43] G. Asryan et al., Nucl. Instrum. Methods Phys. Res., Sect. A 959, 163425 (2020).
- [44] D. S. Carman *et al.*, Nucl. Instrum. Methods Phys. Res., Sect. A 960, 163629 (2020).
- [45] S. Boyarinov et al., Nucl. Instrum. Methods Phys. Res., Sect. A 966, 163698 (2020).
- [46] B. Raydo et al., Nucl. Instrum. Methods Phys. Res., Sect. A 960, 163529 (2020).
- [47] V. Ziegler et al., Nucl. Instrum. Methods Phys. Res., Sect. A 959, 163472 (2020).
- [48] R. Capobianco *et al.*, CLAS12-Note 2023-001 (2023), https://misportal.jlab.org/mis/physics/clas12/viewFile.cfm/ 2023-001.pdf?documentId=83.
- [49] M. Ungaro *et al.*, Nucl. Instrum. Methods Phys. Res., Sect. A 959, 163422 (2020).
- [50] S. S. Agostinelli *et al.*, Nucl. Instrum. Methods Phys. Res., Sect. A **506**, 250 (2003).
- [51] M. Sargsyan, CLAS-NOTE 90-007 (1990), https://www.jlab. org/Hall-B/notes/clas_notes90/note90-007.pdf.
- [52] L. W. Mo and Y. S. Tsai, Rev. Mod. Phys. 41, 205 (1969).
- [53] S. Stepanyan *et al.*, CLAS12-Note 2020-005 (2020), https://misportal.jlab.org/mis/physics/clas12/viewFile.cfm/2020-005.pdf?documentId=70.
- [54] AAO_GEN event generator https://github.com/JeffersonLab/aao_gen
- [55] L. Brenner et al., Int. J. Mod. Phys. A 35, 2050145 (2020).
- [56] G. D'Agostini, Nucl. Instrum. Methods Phys. Res., Sect. A 362, 487 (1995).
- [57] RooUnfold github repository, https://gitlab.cern.ch/RooUnfold/ RooUnfold.
- [58] H. Avakian and P. Bosted, CLASDIS event generator, https://github.com/JeffersonLab/clasdis/blob/master/README.md.
- [59] G. Ingelman, A. Edin, and J. Rathsman, Comput. Phys. Commun. 101, 108 (1997).
- [60] P. Bosted, CLAS-Note 2004-005 (2004), https: //misportal.jlab.org/ul/Physics/Hall-B/clas/viewFile.cfm/2004-005.pdf?documentId=54
- [61] R. Fair et al., Nucl. Instrum. Methods Phys. Res., Sect. A 962, 163578 (2020).
- [62] G. V. Fedotov *et al.* (CLAS Collaboration), Phys. Rev. C 98, 025203 (2018).
- [63] G. Ricco et al., Nucl. Phys. B 555, 306 (1999).
- [64] A. A. Golubenko, V. V. Chesnokov, B. S. Ishkhanov, and V. I. Mokeev, Phys. Part. Nuclei 50, 587 (2019).
- [65] Structure function and cross-section interface website, https:// clas.sinp.msu.ru/strfun/.
- [66] CLAS Physics Database, http://clasweb.jlab.org/physicsdb.
- [67] R. L. Workman *et al.* (Particle Data Group), Prog. Theor. Exp. Phys **2022**, 083C01 (2022).
- [68] V. I. Mokeev et al., Phys. Lett. B 805, 135457 (2020).
- [69] A. Accardi et al., Eur. Phys. J. A 60, 173 (2024).
- [70] S. J. Brodsky et al., Int. J. Mod. Phys. E 29, 2030006 (2020).
- [71] M. Ding, C. D. Roberts, and S. M. Schmidt, Particles 6, 57 (2023).